MIT Open Access Articles

Lithium Concentration from Salt-Lake Brine by Donnan-Enhanced Nanofiltration

Massachusetts Institute of Technology

Lithium Concentration from Salt-lake Brine by Donnan-enhanced Nanofiltration

Zi Hao Foo,[†,‡] Danyal Rehman,[†,‡] Andrew T. Bouma,[†] Sebastian Monsalvo,[†] and John H. Lienhard[*,†]

†*Department of Mechanical Engineering, Massachusetts Institute of Technology, Cambridge, Massachusetts 02139, United States*

‡*Center for Computational Science and Engineering, Massachusetts Institute of Technology, Cambridge, Massachusetts 02139, United States*

E-mail: lienhard@mit.edu

Abstract

Membranes offer a scalable and cost-effective approach to ion separations for lithium recovery. In the case of salt-lake brines, however, the high feed salinity and low pH of the post-treated feed have an uncertain impact on nanofiltration's selectivity. Here, we adopt experimental and computational approaches to analyze the effect of pH and feed salinity, and elucidate key selectivity mechanisms. Our dataset comprises over 750 original ion rejection measurements, spanning five salinities and two pH levels, collected using brine solutions that model three salt-lake compositions. Our results demonstrate that the Li^+/Mg^{2+} selectivity of polyamide membranes can be enhanced by 13 times with acid pre-treated feed solutions. This selectivity enhancement is attributed to the amplified Donnan potential from the ionization of carboxyl and amino moieties under low solution pH. As feed salinities increase from 10 to 250 g L^{-1}, the Li^+/Mg^{2+} selectivity decreases by $\sim$43 %, consequent of weakening exclusion mechanisms. Further, our analysis accentuates the importance of measuring separation factors using representative solution compositions, to replicate the ion transport behaviors with salt-lake brine. Consequently, our results reveal that predictions of ion rejection and Li^+/Mg^{2+} separation factors can be improved by up to 80 % when feed solutions with the appropriate Cl^-/SO_4^{2-} molar ratios are used.

Keywords: Hypersaline Brine, Lithium Extraction, Nanofiltration, Resource Recovery, Selectivity Mechanism

2

Synopsis

Membrane processes play an instrumental role in the green transition, allowing critical materials to be harvested sustainably from hypersaline brine.

1 Introduction

In an era of accelerating resource scarcity fueled by climate change and population growth, the development of sustainable separation systems capable of accessing non-traditional sources of critical minerals is of paramount importance.[1–3] Owing to its high electrochemical activity and heat capacity, lithium is the central component of modern-day batteries and is a resource of increasing strategic importance for most economies.[4,5] In spite of its abundance in continental and geothermal salt-lakes, the price of lithium is inelastic, owing to its production using conventional evaporation ponds.[6,7]

To avoid the slowness and land requirements of evaporation ponds, lithium can instead be produced from salt-lake brines using direct lithium extraction (DLE).[8] In DLE, adsorbents or chelating agents separate Li^+ ions from a multicomponent aqueous mixture (e.g., Na^+, K^+).[4,8] The high concentration of divalent ions in salt-lake brines (such as Mg^{2+}), however, inhibits and attenuates DLE's separation efficiency due to their similar ionic radii (0.76 Å for Li^+, 0.72 Å for Mg^{2+}).[4,6] To improve lithium yield and purity, the hypersaline feed can be pre-treated to selectively eliminate multivalent ions, leveraging solvent extraction,[9,10] nanofiltration,[11,12] selective electrodialysis,[13–15] chelating agents,[16,17] or other absorption-based methods.[1] Nanofiltration, in particular, is attractive for brine softening owing to its high energy and separation efficiencies, reliability, and ease of scalability.[12,18–20]

Traditional nanofiltration membranes are typically thin-film composites comprising a polyamide selective layer, and a polysulfone support layer.[20–23] The polyamide layer is conventionally fabricated through interfacial polymerization between trimesoyl chloride and piperazine, and the membrane's permeability and ion selectivity are dictated by the degree of crosslinking.[24] Consequently, electrostatic potentials form along the membrane-liquid interface during operation, resulting from the ionization of residual carboxyl and amino moieties in polyamide matrix with water.[21,25–27] Ion fractionation of the feed solution is achieved through a combination of steric, dielectric and Donnan exclusion mechanisms.[19,28–31] In re-

4

cent demonstrations, the monovalent cation selectivity can be effectively enhanced by up to six times with Donnan potential magnification, through active layer functionalization with positive charge centers or surface coatings. [32–37]

The challenge of Li^+/Mg^{2+} separation with nanofiltration has received sustained interest in the literature. [3,4,38,39] The majority of salt-lake brines are multicomponent and have high feed salinities. However, most prior studies tend to focus on dual cation feed solutions (i.e., Li^+ and Mg^{2+} cations) that are lower in concentrations, and which do not necessarily replicate the transport dynamics in actual multicomponent salt-lake brine. [34–37,40–42] As we will demonstrate, the apparent ion rejections and Li^+/Mg^{2+} separation factors vary by up to 80 % and 40 %, respectively, between experiments involving dual cation solutions and concentrated salt-lake brines. Furthermore, as a prerequisite for brine valorization, the feed solution is acid pre-treated in the industry to mitigate carbonate and silicate scaling; [4,43] the effect of lowering feed solution pH on the membrane's monovalent selectivity and ion permeability under high salinities is nuanced and remains unclear. [21]

In this study, we analyze the kinetics of ion transport across polyamide NF membranes, elucidating the dependence of the ion selectivity and water permeability coefficient on intrinsic membrane parameters, feed composition, salinity and pH level. Over 750 original ion rejection measurements, spanning five salinities and two pH levels, are recorded using brine solutions that model the compositions of three salt-lakes. The measured data is used to calibrate a semi-empirical model and systematically tabulated in the SI for future reference. To deconvolute the highly coupled transport phenomena, [44] we juxtapose the rejection data with dual cation and multicomponent feed solutions, pinpointing specific ion-membrane and ion-ion interactions that give rise to differences in apparent selectivities. Lastly, we discuss possible mechanisms for the observed weakening of selectivities at higher feed salinity and the importance of choosing representative feed solutions for membrane characterization.

2 Materials and Methods

2.1 Materials and Chemicals

Synthetic brine solutions were prepared based on the aqueous salt-lake composition of Salar de Atacama, Chile,[18] Qaidam Lake, China[19] and Salton Sea, United States,[45] as given in Table 1. To investigate salinity effects, diluted variants of the respective brines were prepared while keeping the relative ionic ratios constant (see Supp. Tables 1 – 3 in SI). To ascertain the influence of multicomponent effects on the ion selectivity, complementary experiments with dual cation solutions comprising Li^+ and Mg^{2+} ions were conducted (see Supp. Table 8 in SI). Deionized water from an in-house reverse osmosis system was used in the preparation of all stock solutions. ReagentPlus-grade NaCl, KCl, LiCl, $MgCl_2$, $CaCl_2$, Na_2SO_4, K_2SO_4, Li_2SO_4, $MgSO_4$, $CaSO_4$ (anhydrous, >99 %), NaOH (anhydrous, >98 %) and HCl (37 %) were procured from MilliporeSigma. Semi-aromatic polyamide nanofiltration (NF) membranes, and the feed and permeate channel spacers, were obtained from commercial spiral-wound modules (DuPont FilmTec NF270–2540). The NF membranes were stored in a buffered 1 wt% $Na_2S_2O_5$ solution, and soaked in deionized water for 24 h before use. The membranes have a nominal molecular weight cutoff (MWCO) between 200 and 400 Da, and they are stable for continuous operation between the pH levels of 2 – 11.

Table 1: Nominal ionic composition of the synthetic hypersaline brine from major commercial salt-lake reservoirs.

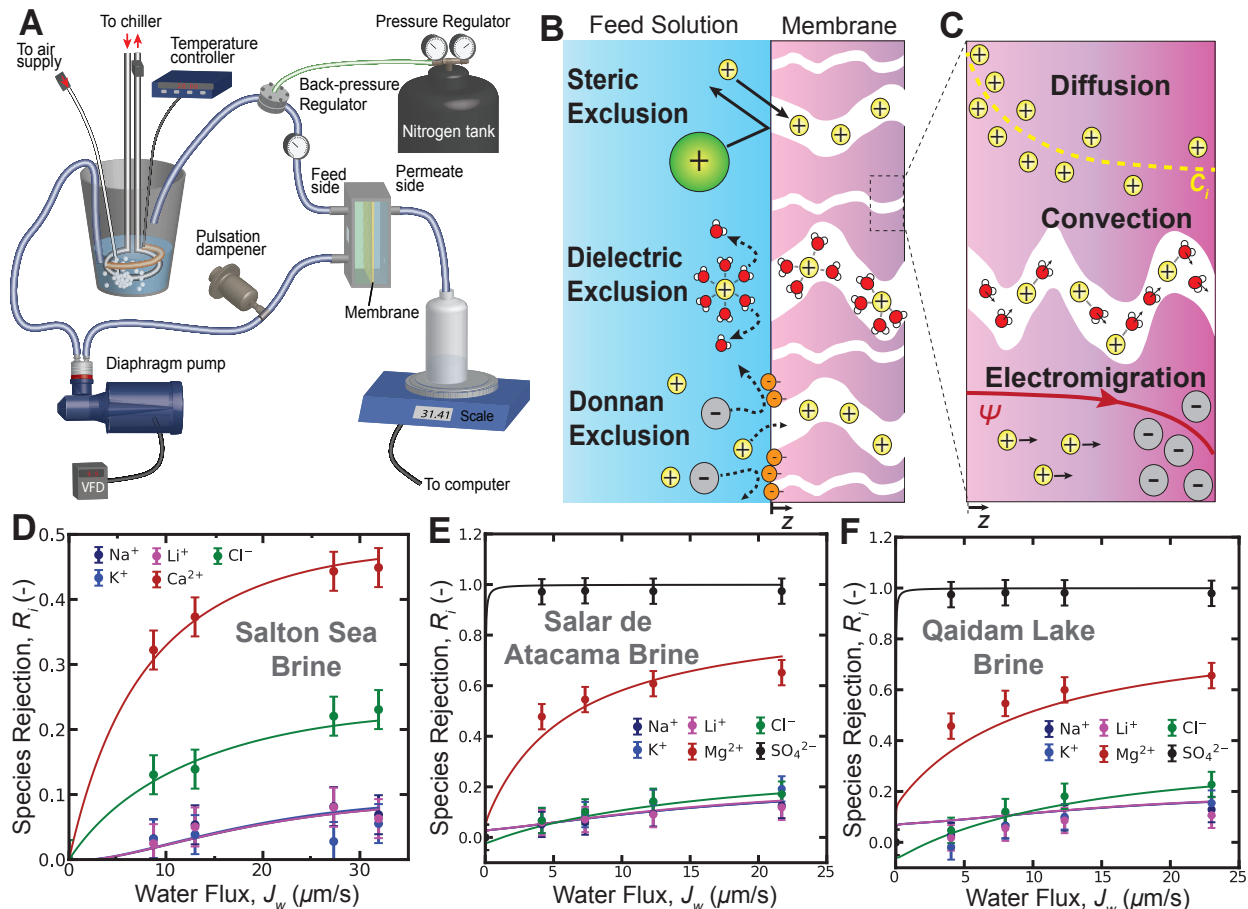| Salt Lake, Location	Nominal Composition (g L^{-1})							
	Li$^+$	Na$^+$	K$^+$	Mg^{2+}	Ca^{2+}	Cl$^-$	SO$_4^{2-}$	TDS
Salar de Atacama, Chile[18]	1.19	69.01	17.89	7.31	–	143.72	12.06	251.18
Qaidam Lake, China[19]	0.31	56.30	4.40	20.20	–	134.20	34.10	249.51
Salton Sea, United States[45]	0.22	53.70	17.10	-	26.30	152.00	0.12	249.44

Figure 1: **A**) Schematic diagram of the bench-scale nanofiltration experimental setup, including the pressure module and permeate measurement and collection system;[46] **B**) Selectivity mechanism for salt partitioning into the nanofiltration membrane pore, including steric, dielectric and Donnan exclusion mechanisms. The membrane's active layer is modeled as a network of continuous and tortuous nanoscale water channels, based on pore flow models;[47] **C**) Transport mechanisms and their respective driving forces for ionic transport across the nanofiltration membrane, including convective, diffusive and electromigrative contributions; Experimental measurements and computational predictions of species rejection for multi-component salt-lake brine from **D**) Salton Sea, United States, **E**) Salar de Atamaca, Chile and **F**) Qaidam Lake, China.

2.2 Experimental Apparatus

A plate-and-frame bench-scale cross-flow membrane module was adopted to characterize the performance of the polyamide membrane (Figure 1A).[46] The custom-built module had flow channel dimensions of 8.0 cm in length, 3.0 cm in width and 1.0 mm in thickness, and was capable of accommodating up to 70 bar of feed pressure. Cross-flow was maintained

7

using positive displacement pumps (Hydra-Cell F20). A pulsation dampener (Hydra-Cell 4CI SST) was installed upstream of the membrane module to negate pressure pulsations. Pressure transducers with 1 % reading uncertainty (Wika A-10) were installed along the feed and permeate flow streams to monitor the flow pressure in real-time on the LabView software. The water flux was determined by gravimetry, using a digital mass scale with 0.1 g readability (Ohaus Scout Pro SP601). The solution conductivity and pH levels were monitored and recorded at 1 Hz frequency (Hach HQ440d). Streaming potential experiments were conducted with the Anton Paar SurPASS 3 zeta potential system.

2.3 Membrane Performance Tests

Over 750 ion rejection measurements, based on 144 water samples from distinct operating conditions, were recorded using dual cation and multicomponent salt-lake brines (see Supp. Table 1 – 9 in SI). The experiments were conducted at a cross-flow velocity of 0.17 m s^{-1}, and at a temperature of 20.0 ± 0.5 °C. The total dissolved solids (TDS) concentration of the feed solution ranges between 10 and 250 g L^{-1}, at pH levels of 2 and 7, to assess the impact of acid pretreatment on ion selectivity. In light of bicarbonate and carbonate scaling risks in lithium extraction applications, alkaline feed conditions were not investigated.[4,14] In these experiments, the membrane coupon was installed and compacted at an applied pressure of 8 bar with deionized water for 2 h. Thereafter, the membrane coupon was equilibrated with the salt solution for 15 mins at the specific pressure before sample collection. Solution pH levels were adjusted with dropwise addition of 1 M HCl and 1 M NaOH. The feed and permeate samples were collected in centrifuge tubes and chilled. The ionic compositions of the solutions were analyzed with inductively coupled plasma optical emission spectroscopy (Agilent ICP-OES 5100), calibrated using three-point standards from MilliporeSigma (Trace-Cert). The maximum uncertainty in each concentration measurement was under 2 %, based on triplicate measurements.

The water flux was calculated by measuring the change in the mass of the permeate

8

solution, according to Eq. 1.

$$J_w = \frac{\Delta m}{\rho_w A_m \Delta t} \tag{1}$$

where J_w (L m^{-2} h^{-1}, i.e., LMH) denotes the water flux, Δm and Δt denote the change in mass (g) and time (h), ρ_w denotes the density of water (g L^{-1}), and A_m denotes the effective membrane area (m^2).

The membrane's water permeability coefficient was calculated by averaging the ratio of the pure water flux over the applied pressure, across feed pressures ranging from 5 to 40 bar. The flow loop volume was calibrated and incorporated to prepare the feed solutions (see text A.1 in SI). The ion rejections were calculated with Eq. 2, using concentrations determined by ICP-OES.

$$R_i = 1 - \frac{C_{i,p}}{C_{i,f}} \tag{2}$$

where R_i denotes the rejection of ion i (-), $C_{i,f}$ and $C_{i,p}$ denote the species concentration in the feed and permeate solution (g L^{-1}).

Lastly, the selectivity separation factor between solutes i and j was calculated with Eq. 3.

$$\alpha_{i/j} = \frac{C_{i,p}/C_{j,p}}{C_{i,f}/C_{j,f}} \tag{3}$$

where $\alpha_{i/j}$ denotes the separation factor between solutes i and j (-).

2.4 Transport Model

The Donnan-steric pore model with dielectric exclusion (DSPM-DE) was used as a computational tool to complement the experiments in inferring solute partitioning behavior, and to characterize transmembrane species transport.[47] A full description of the model, including the numerical assumptions, limitations and the solution algorithm, appears in the Supporting Information (see text B.1 in SI). The DSPM-DE model neglects active layer heterogeneity,[26,48] assumes full dissociation of the inorganic salts[29] and models the dissolved

9

solutes based on its hydrodynamic radii.[20] Despite its limitations, the model can predict the transport coupling between the ions arising from charge anisotropy,[49–51] provide order-of-magnitude estimations for the transport and partitioning mechanisms,[27,52] and reproduce the asymptotic rejection behaviors observed under high Péclet numbers.[21,22,28] A complete list of the model assumptions and implications is delineated in the SI.

The extended Nernst-Planck equation was used to model species transport arising from diffusion, convection and electromigration in DSPM-DE, and are provided in Eq. 4 and illustrated in Figure 1C. Here, the water flux was measured experimentally and served as a model input.

$$J_i = K_{i,a}c_i J_w - K_{i,d}D_{i,\infty}\nabla c_i - K_{i,d}D_{i,\infty}\frac{z_i c_i F}{RT}\nabla\Psi \tag{4}$$

where J_i denote the solute flux (mol m^{-2} h^{-1}), $K_{i,a}$ and $K_{i,d}$ denote the hindrance coefficients from convection (-) and diffusion (-), c_i and z_i denote the molar concentration (mol L^{-1}) and electronic valency (-), $D_{i,\infty}$ denotes the Fickian diffusion coefficient (m^2 s^{-1}), F and R denote the Faraday (C mol^{-1}) and ideal gas constants (J mol^{-1} K^{-1}), and T and Ψ denote the temperature (K) and electric potential (V).

To ensure chemical stability, electroneutrality conditions are imposed on the solution in the bulk and within the membrane pores, as provided by Eq. 5 and 6, respectively.

$$\sum_{i}^{N} z_i c_i = 0 \tag{5}$$

$$\chi_d + \sum_{i}^{N} z_i c_i = 0 \tag{6}$$

where χ_d represents the charge density of the active layer (mol m^{-3}).

To ensure that the Gibbs free energy remains continuous, isoactivity conditions were imposed along the solution-membrane boundary.[23,53] The solute's effective partition coefficient, consequently, was defined as the ratio of the solute activity within the membrane to the bulk solution, as provided in Eq. 7. Here, solute partitioning was the result of steric, dielectric

and Donnan exclusion mechanisms, as illustrated in Figure 1B (see text B.1 in SI).

$$\frac{(\gamma_i c_i)_{mem}}{(\gamma_i c_i)_{bulk}} = \Phi_{i,steric} \ \Phi_{i,Donnan} \ \Phi_{i,dielectric} \tag{7}$$

where γ_i denotes the activity coefficient of solute i, and Φ_i denotes the partition coefficient.

The formation of concentration boundary layers on the membrane surface impacts the apparent membrane selectivity.[54] To incorporate the concentration polarization effects, the boundary layers were modeled using the method developed by Geraldes and Alves, incorporating diffusive, convective and electromigrative effects[47,49] (see text B.2 in SI). Mass transfer coefficients within the concentration boundary layers were calculated using empirical correlations from our prior study.[55] The governing differential equation for species and charge conservation were discretized and solved, using numerical solvers developed in Python (see text B.1 in SI). The four model parameters, i.e., the average pore radius, effective membrane thickness, charge density and the relative permittivity of water within the pores, were regressed from 72 ion rejection measurements, for each solution pH. The optimization problem was solved with a metaheuristic stochastic minimization algorithm,[56] and the results are summarized in Supp. Table 10.

3 Results and Discussion

3.1 Membrane Characterization and Model Calibration

To calibrate the consistency of DSPM-DE, we compared the predicted ion rejections from the model to the experimental results by Micari et al.,[57] and Labban et al.,[49] using original model parameters from the respective authors (see text B.3 in SI). The maximum absolute deviations were below 15 % and 8 % for the two cases. Furthermore, the model captured the effects of ionic coupling, reproducing the negative rejection phenomena observed for small monovalent ions.[28,50]

11

Next, the original ion rejection measurements of the present work were used to calibrate the model parameters of DSPM-DE, allowing us to infer differences in the solute transport between the dual cation and multicomponent brines. Mindful of the assumptions and limitations of DSPM-DE, we restricted its use to brines of low concentrations (10 g L^{-1}), avoiding ion-pairing[58,59] and coupled diffusion[60,61] phenomena that occur at higher concentrations. Further, the model was calibrated to 72 ion rejection measurements from three unique brine compositions (see Supp. Table 1 – 3 in SI), to prevent overfitting of the 4 model parameters. The agreement between the model and multicomponent brine experiments at pH 7 is exemplified in Figure 1C – E, with a normalized root-mean-square error of 2.8 %. Similar agreement was obtained for the experiments with multicomponent solutions at pH 2, and with dual cation solutions, as shown in Supp. Figure 4 and 5.

Subsequently, we compared our numerical parameters to prior empirical membrane characterizations. The pore radius of NF 270 has been reported to be between 0.43 to 0.54 nm,[57,62–65] and the pore size distribution has been estimated to be approximately 0.3 ± 0.1 nm, based on MWCO experiments.[24] In comparison, DSPM-DE suggested pore radii of 0.416 and 0.461 nm, at pH 7 and 2, which were within the error of the reported estimates. Using the model parameters at pH 7, the predicted limiting rejections for glucose, sucrose and raffinose were within 8.5 % of the empirical measurements.[49] Using a LiCl binary solution, DSPM-DE predictions for its partition coefficient were 0.176, approximately 16.2 % lower than the expected value of 0.21 ± 0.06 obtained from earlier quartz crystal microbalance with dissipation (QCM-D) measurements.[66] The predicted relative permittivity within the pores was 39.58, which was within 6 % of the best estimates in the literature.[49,50,57]

3.2 Donnan Exclusion enhances Monovalent Selectivity

We leveraged our calibrated model to examine the monovalent selectivity of nanofiltration, inferring key partitioning and transport mechanisms for $\text{Li}^+/\text{Mg}^{2+}$ separation. Electrostatic potentials form along the solution-membrane interface because the carboxyl and amino func-
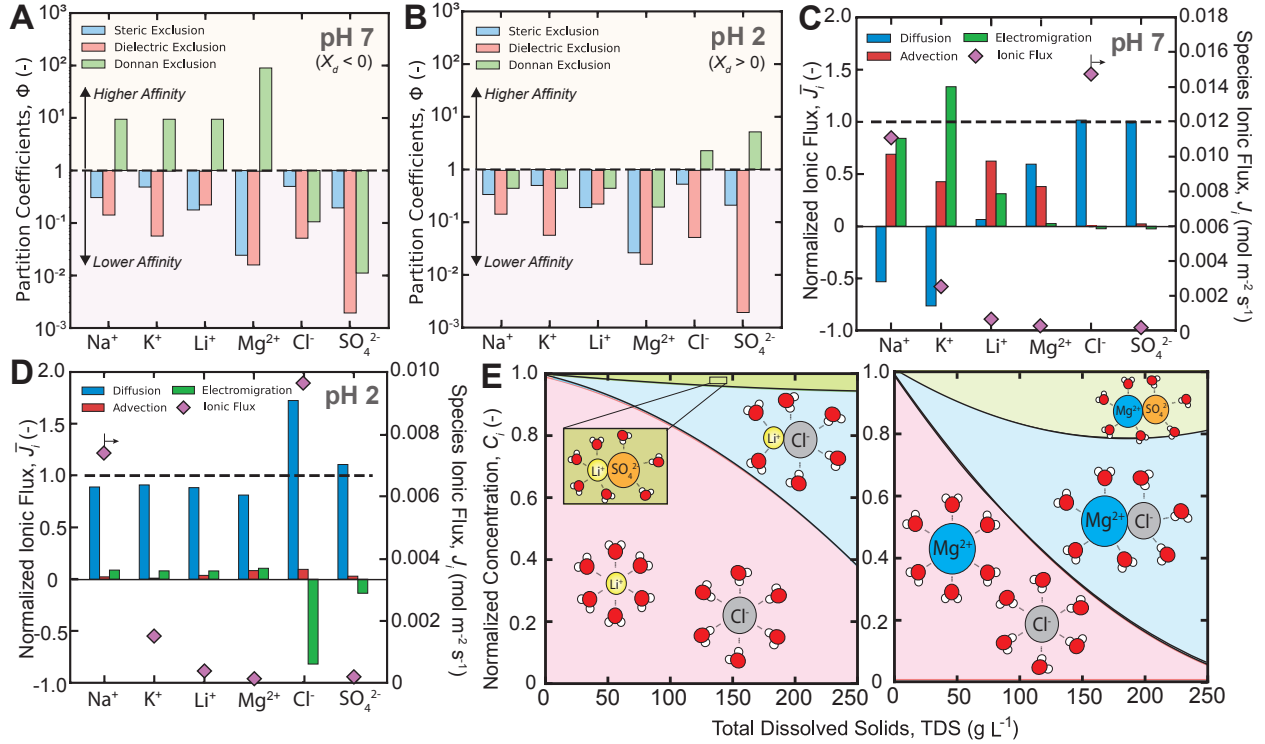
Figure 2: Schematic diagrams of the thermodynamic partition coefficients and the transport mechanisms for the ionic species in the Chilean brine, at a total dissolved solids concentration of 10 g L^{-1}. Note that the partition coefficients are plotted on a logarithmic scale, and are compared at the same water flux of 15 L m^{-2} h^{-1}. The relative contributions from steric, dielectric and Donnan exclusions, at a solution pH of **A**) 7 and **B**) 2, are outlined in blue, red and green, respectively. A partition coefficient lower than 1 (dotted lines) indicates selective rejection, and vice versa. Schematic diagrams for the diffusive, convective and electromigrative fluxes normalized to the total ionic flux of each species (left vertical axes) at a transmembrane water flux of 15 L m^{-2} h^{-1}, at solution pH of **C**) 7 and **D**) 2, respectively. The normalized fluxes from the constituent mechanisms sum to 1 (dotted line). The extensive ionic fluxes are plotted on the right vertical axes to illustrate relative permeate concentrations. The results suggest transport coupling between cations and anions, induced through charge anisotropy across the active layer, to maintain solution electroneutrality. **E**) Solution speciation in Chilean brine as a function of increasing TDS. At high concentrations, ion-pair complexes between Li$^+$, Mg^{2+}, Cl$^-$ and SO$_4^{2-}$ dominate,[58,67] impacting NF selectivity due to attenuated solvation energy differences between species.

tional groups tend to ionize in water.[68,69] The isoelectric point (IEP) is defined as the pH

level that corresponds to a neutral active layer.[29,70] Here, we experimented under neutral

and acidic conditions, corresponding to solution pH levels above and below the IEP. Feed

solutions at pH 2 were selected to mimic the effects of acid pre-treatment in resource recov-

13

ery applications.[7,43]

The schematic diagrams for the derived partition coefficients from steric, dielectric and Donnan exclusion are presented in Figure 2A and B, using the Chilean brine at 10 g L^{-1}. The analyses for the other tested compositions are provided in the SI (see text C.1 in SI). We note that the partition coefficients are plotted on logarithmic axes to accentuate the differences in the exclusion mechanisms. The derived partition coefficients suggested that the active layer was ion rejecting, which was consistent with prior knowledge of semi-aromatic polyamide membranes.[71] Between the six ions, the trend in the magnitudes of steric and dielectric exclusion aligned with literature predictions from hindered transport[50] and solvation theories surrounding ion dehydration,[51,67,72] respectively.

From the experiments, the rejection of multivalent cations increased from 55 to 97 % approximately, when the solution pH was lowered from 7 to 2. The rejection of monovalent cations, however, rose incrementally by 15 % on average, amplifying the separation factor between Li$^+$ and Mg^{2+} by a factor of six. Using our transport model, we attributed this phenomenon partly to changes in the ion partitioning behavior, as a result of the membrane's Donnan potential increasing with the protonation of the carboxyl and amino moieties,[69] yielding a positive surface potential. This result is corroborated by zeta potential measurements of the active layer, as presented in Supp. Figure 6. Cations that previously permeated under the negative Donnan potential now encountered an amplified energy barrier from the positive Donnan potential.[27,73] This conclusion is corroborated by Figure 2A and B and Supp. Table 12, where the derived partition coefficients from Donnan exclusion that were originally greater than 1 at pH 7, fell to be consistently below 1 at pH 2. For the anions, conversely, the model predicted an increase in permeation from the Donnan potential changes, reproducing the observed reductions in SO$_4^{2-}$ rejections from the experiments. Smaller ions with higher charge densities, i.e., multivalent cations, were impacted to a greater extent by the electrostatic effects.[27] This disparity between ions amplified the rejection of multivalent cations disproportionately, elevating Li$^+$/Mg^{2+} separation factors. Our findings

reemphasized that the strength of Donnan exclusion, from the ionized charged groups in the polyamide matrix, is highly sensitive to solution pH, and can be optimized for the ion selectivity of nanofiltration.

3.3 Ion Transport Coupling attenuates under Low Solution pH

The literature contains copious evidence of ionic coupling in transmembrane transport,[2,44,60,74,75] although prior studies focused largely on simple pore geometries and dual cation solutions. Here, the effects of transport coupling on ionic fluxes were evaluated using multicomponent salt-lake brines, as illustrated in Figure 2C and D.

Across all three tested compositions at pH 7 (see text C.2 in SI), our model suggested that Cl^- ion transport was largely diffusive, as depicted in Figure 2C.[29] This was a consequence of the stronger Donnan exclusion effects on Cl^- at pH 7, lowering the effective partition coefficient, and establishing a relatively large concentration gradient across the active layer, as depicted in Supp. Table 12, and Supp. Figure 8. Under steady-state conditions, consequently, the large ionic flux of Cl^- resulted in charge anisotropy, inducing a reverse electric potential across the active layer.[74,76] The induced electric field, conversely, accelerated the transport of monovalent cations (Li^+, Na^+, K^+) to preserve electroneutrality, coupling the two transport rates by electromigration, as illustrated in Figure 2C. This deduction corroborates with prior molecular dynamics simulations[69,74] and multi-ionic experiments.[27,50] However, the multivalent ions (Mg^{2+}, Ca^{2+}) were inhibited by its lower partitioning rates, causing the ionic fluxes to be one order of magnitude lower than the monovalent ions. Consequently, as informed by our computational models in Figure 2C, we inferred that the influence of electromigrative coupling was less prominent for multivalent cations.

Under acidic conditions at pH 2, our experiments suggested that the water permeability coefficient decreased by approximately 40 %. Recent experiments attributed the permeability change to a physical restructuring of the polyamide matrix.[77] Assuming a 20 nm thick polyamide layer, likewise, our model suggested a reduction in the porosity-tortuosity factor

15

by 23 %. Consequent of the denser active layer, as illustrated in Figure 2D, the absolute flux of each ion fell by 45 % from weakening convective and electromigrative coupling. Therefore, our model suggests that the ionic transport is largely driven by diffusion under low pH.

3.4 Membrane Selectivity lowers with Multicomponent Brine

Figure 3A illustrates the trade-off between the water permeability coefficient and the Li^+/Mg^{2+} selectivity, comprising data on commercial and lab-scale membranes functionalized with charge centers.[34–37,40–42] To be consistent with prior work, dual cation feed solutions containing 1000 ppm LiCl and 2000 ppm $MgCl_2$ were used to determine the separation factors in Figure 3A. Following the protonation of carboxyl and amino moieties within the polyamide matrix under acidic environments, our experiments revealed that the Li^+/Mg^{2+} selectivity of NF 270 can be significantly enhanced, from 2.15 to 39.1. As a result of the Donnan exclusion enhancements, the monovalent selectivity of NF 270 approached the performance of the functionalized membranes on the trade-off plot.[33,34,37,78] These findings revealed that a synergy between the solution pH and membrane functionalization may be derived, offering an additional sensitive optimization parameter for the monovalent selectivity of next-generation NF membranes.

Figure 3B – F illustrate the effects of feed salinity and solution pH on the monovalent selectivity of nanofiltration, based on experiments with three multicomponent salt-lake brines.[18,19,45] The separation factors are calculated based on the largest experimental water flux, to simulate comparisons based on either their asymptotic ion rejections, or at the hydraulic pressure limits of the membrane.[20,28] Compared to the Chilean and Chinese salt-lake brines, we found that the derived Li^+/Mg^{2+} separation factors were overestimated by 40 % when the dual cation solutions from prior work in Figure 3A were used; these results highlighted the strong influence of multicomponent effects on the apparent monovalent selectivity of NF, underscoring the need to characterize membranes with representative compositions of the respective brines.
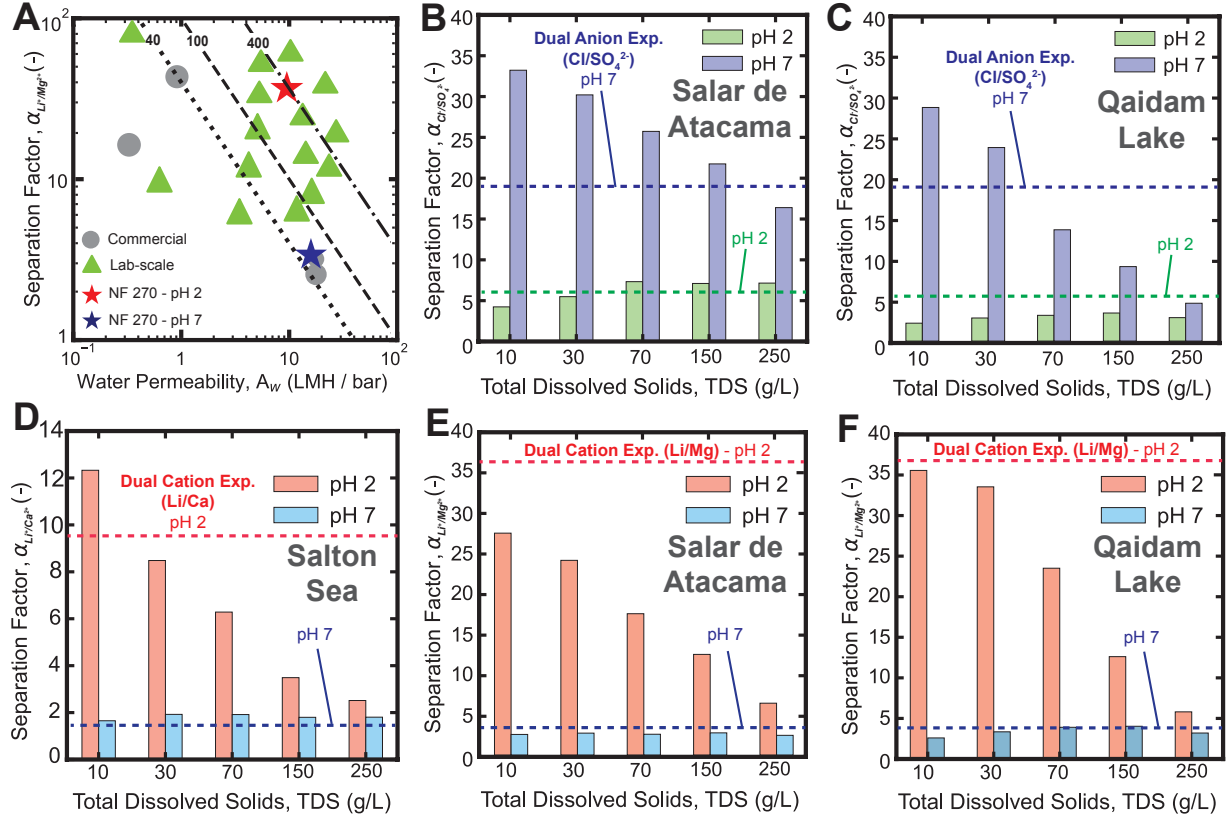
16

Figure 3: **A**) Robeson plot between the separation factor and water permeability coefficient of nanofiltration membranes, at the best performing solution pH, as reported in the literature.[34–37,40–42] Here, NF 270 was evaluated using LiCl-MgCl$_2$ solutions as for the other membranes. Dashed lines represent constant values of $\alpha_{i/j} A_w$, a common metric to quantify the recovery potential of Li relative to Mg.[34] The Li selectivity of NF 270 membranes improves significantly at low solution pH levels (within recommended operating range). Selectivity performance of NF 270 for Cl$^-$/SO$_4^{2-}$ separation, for inorganic brines from **B**) Salar de Atacama, Chile, and **C**) Qaidam Lake, China. For all tested compositions, the Cl$^-$/SO$_4^{2-}$ separation factor remains largely invariant to TDS changes at pH 2, while exhibiting a decreasing trend with increasing TDS at pH 7. Experimental measurements of the selectivity performance of NF 270 for Li$^+$/Mg^{2+} separation, as a function of the solution pH and total dissolved solids (TDS) concentration, for inorganic brines from **D**) Salton Sea, United States, **E**) Salar de Atacama, Chile and **F**) Qaidam Lake, China. For all tested compositions, the effect of solution pH on the selectivity of Li$^+$/Mg^{2+} separations are opposite to the trends for the anionic separation. Separation factors are calculated at the largest experimented water flux, to simulate comparisons based on either their asymptotic ion rejections, or near the respective hydraulic pressure limits of the membrane.[20,28] The dotted lines in (B) - (F) denote the separation factors obtained with LiCl-MgCl$_2$ solutions, following conventions in the literature.[34–37,40–42]

17

Further, below the IEP (pH 2), influenced by a positive polyamide charge density, we observed that the Li^+/Mg^{2+} separation factors decreased with increasing TDS concentrations; the Li^+/Mg^{2+} separation factors attenuated from 27.2 and 35.7 at 10 g L^{-1}, to 6.32 and 5.81 at 250 g L^{-1}, for the Chilean and Chinese brines, respectively. The separation factors of the cations, however, remained largely invariant with increasing TDS concentrations when the pH is above the IEP. Conversely, the opposite relationship between Cl^-/SO_4^{2-} separation factors and TDS concentration was observed, for both pH. The precise mechanism for the decline in monovalent selectivity at high salinities remains unclear for NF. However, coupled with the measured reductions in ion rejection (see Supp. Table 5 – 7 in SI), the results suggested that the weakening of dielectric and Donnan exclusions were plausible factors for the observed decline.

In recent publications, the average hydration number of ions was observed to decrease in nanoscale channels.[12,25,30] Within the membrane pores, ions partially dehydrate from the nanoscale confinement, lowering the dielectric constant and presenting an energy barrier for ion transport.[2] At higher ionic salinities, however, stable ion-pairs form between oppositely-charged ions, reducing the effective hydration numbers in the solution, as described in Figure 2E.[58] It is likely that the ion-pair formation narrowed the energy differences for ion dehydration between monovalent and divalent cations, weakening and minimizing the differences in dielectric exclusion.[67] Further, at higher salinities, the electric double layer on the channel walls is thinner, spanning less of the channel cross-section and lowering the effective activation energies for ion conductance from charge screening.[15,68] This was accompanied by an attenuation of the surface charge density, as suggested by zeta potential measurements in Supp. Figure 6. The high salinities typical of salt-lake brine suppressed charge-exclusion effects across the solution-membrane interface, thereby elevating the permeability of multi-valent ions and lowering the net monovalent selectivity.
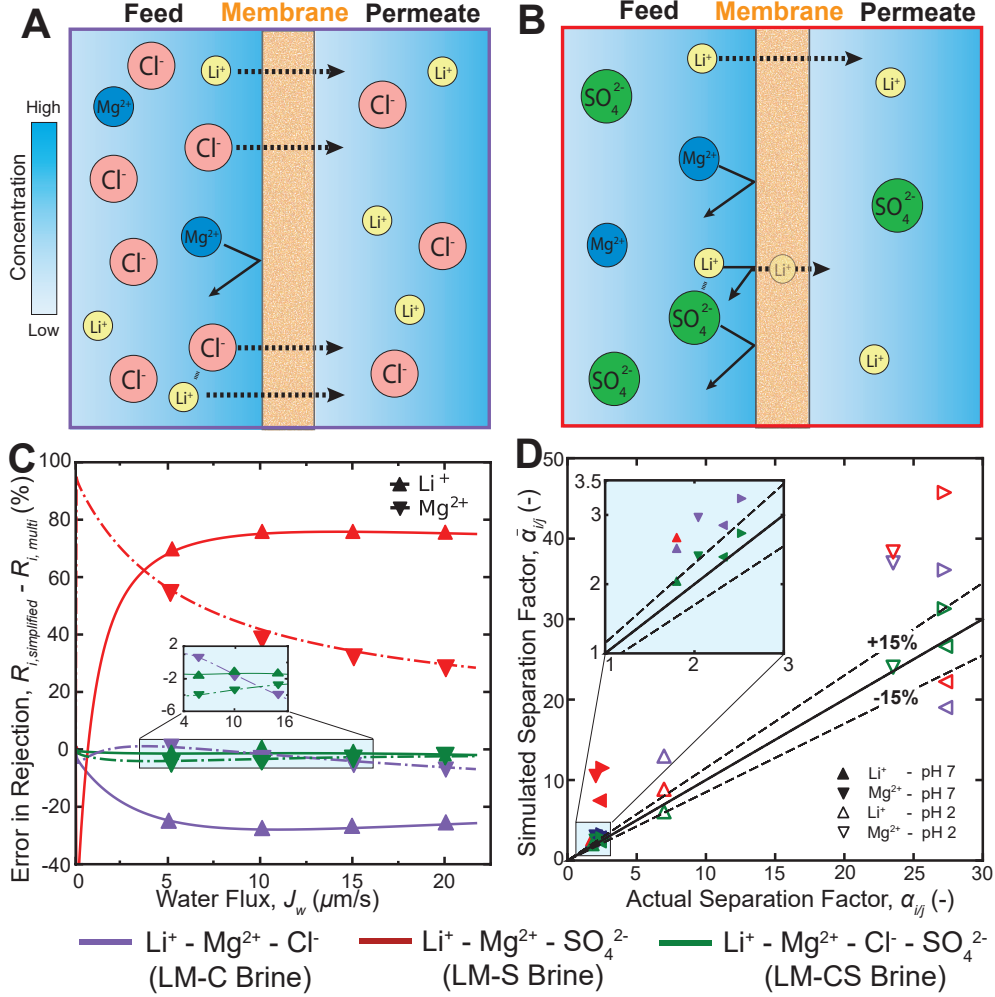
Figure 4: Schematic diagrams illustrating nanofiltration transport coupling with dual cation feed solutions. Here, feed solutions are dual cation if it contains only two cation species (Li^+ and Mg^{2+}), and are multicomponent if it consists of more than two cation species. **A**) Nanofiltration experiments with Li^+–Mg^{2+}–Cl^- (LM-C) brine. The high permeability of Cl^- ions entrains additional cations to permeate through the active layer to maintain electroneutrality. Here, the higher effective partition coefficient of Li^+ causes it to permeate selectively over Mg. **B**) Nanofiltration experiments with Li^+–Mg^{2+}–SO_4^{2-} (LM-S) brine. Here, the high rejection of SO_4^{2-} ions reduce the effective permeation of Li^+ ions to maintain electroneutrality of the solutions. **C**) Plot of the error in species rejection against the transmembrane water flux. Simulated brine that mimics both the cation and anion ratios (green lines and markers) register rejection errors of up to 4 % for both Li^+ and Mg^{2+}, while simplified brines with only one anion, Cl^- (purple) or SO_4^{2-} (red), register rejection errors of up to 80 %. **D**) Plot of the separation factor of the simulated brine against that of the actual multicomponent salt-lake brine. The upward, downward, leftward and rightward markers correspond to transmembrane water fluxes of 5.0, 10.0, 15.0 and 20.0 μm s^{-1}, respectively. Comparisons are made between feed solutions with equal ionic molarity and transmembrane water flux.

19

3.5 Anionic Composition impacts Apparent Monovalent Selectivity

In the preceding sections, our results indicated that the kinetics of cation and anion transport are coupled. In the literature, however, dual cation feed solutions were frequently used to characterize new membranes.[34–37,40–42] Here, we analyzed the impact of solution simplifications on the observed ion rejections and Li^+/Mg^{2+} separation factors.

Rejection differences between the dual cation and multicomponent brines for Li^+ and Mg^{2+} at pH 7 are presented in Figure 4C. Solutions with simplified anionic compositions, namely LM-C and LM-S brines, registered rejection errors up to 80 and 25 % for Li^+ and Mg^{2+}, respectively. When the Cl^-/SO_4^{2-} molar ratio was accurately replicated with the LM-CS brine, we observed that the absolute errors for Li^+ and Mg^{2+} fell under 4 % for both ions. Similar behavior under acidic conditions was observed in Supp. Figure 10 (see text C.3 in SI).

In the absence of SO_4^{2-} ions in LM-C experiments, the total anionic flux was overestimated because of the high diffusive and partitioning rates of Cl^- ions (see Supp. Table 12 in SI). An amplified electric potential than that with the multicomponent brine was induced, increasing the transmembrane cationic flux. In Figure 4A, to perserve electroneutrality, more Li^+ was preferentially transported over Mg^{2+} due to its higher partition coefficient, magnifying its apparent permeance.

Conversely, in the absence of Cl^- ions with LM-S experiments, the net anionic flux fell by 80 % approximately due to the poor SO_4^{2-} partitioning. In Figure 4B, Li^+ and Mg^{2+} rejections increased proportionally to ensure permeate solution electroneutrality, accounting for the rejection differences in Figure 4C.

In Figure 4D, the rejection errors were propagated to assess its implications on the apparent separation factors for Li^+/Mg^{2+}. We found that the separation factor was consistently overestimated by up to 40 % for both pH, when feed solutions with simplified anionic compositions were used. Conversely, the separation factor errors were consistently under 15 %

when the Cl^-/SO_4^{2-} molar ratio was accurately replicated in the feed solution. These results revealed potential causalities between the cation-anion transport coupling and the apparent permselectivity. To accurately assess the selectivity for cation separations, membranes should be characterized using solutions with representative anionic compositions, and vice versa.

4   Implications

Membrane processes are key unit operations in resource recovery applications, providing sustainable and cost-effective methods to separate and concentrate lithium from salt-lake brine. However, the impact on selectivity from the high feed salinity and low solution pH typical of post-treated salt-lake brine remains unclear. In this work, nanofiltration experiments are conducted at five feed salinities and two pH levels, using synthetic brine solutions based on the actual aqueous compositions of three salt-lakes. In total, over 750 original ion rejection measurements are systematically recorded, and the data is used to calibrate a semi-empirical pore-flow model to elucidate transport and selectivity mechanisms.

Our experiments show that the Li^+/Mg^{2+} selectivity of polyamide membranes is enhanced by approximately 13 times when acid pre-treated feed solutions are used. Our models attribute this phenomenon to changes in the ion partitioning behavior, as a result of the amplified Donnan potential from carboxyl group protonation. With multicomponent solutions, the Li^+/Mg^{2+} selectivity decreases by $\sim 43\,\%$ as a result of competition from other mobile monovalent ions; these effects are amplified under higher feed salinities due to a combination of ion-pair formation and the narrowing of the overlap in the electric double layers, leading to leakage of co- and multivalent ions.

Further, the transport kinetics between monovalent cations and anions appear to be coupled by the requirement of electroneutrality in the permeate solution. The degree of coupling is suggested to be weaker under low solution pH, as a result of porosity reductions in the polyamide layer from physical restructuring. In the literature, typically, feed solutions

21

with simplified anionic compositions have been used to evaluate Li^+/Mg^{2+} selectivity. Our measurements show that these simplifications result in an overestimation of ion rejection by up to 80 %. Consequently, the apparent Li^+/Mg^{2+} separation factors in the literature have consistently been overestimated by up to 40 %.

In essence, our experimental results underscore the strong influence of salinity and multicomponent effects on the apparent monovalent selectivity of NF, arising from transport coupling and weakening of exclusion mechanisms. To better represent the selectivity of NF membranes in resource recovery applications, it is crucial that feed solutions with representative anionic compositions and salinities be used.

Supporting Information Available

The following files are available free of charge in the Supporting Information.

- Original experimental data for 750 nanofiltration ion rejection and water flux measurements with dual cation and multicomponent brine.

- Model description and numerical methods for nanofiltration transport model.

- Analysis of solute partitioning, transport phenomena and ionic coupling effects.

Acknowledgement

Author Contributions

Z.H. Foo performed the experiments, programmed the numerical models, and conducted the technical analysis. D. Rehman assisted with the numerical modeling. A.T. Bouma and S. Monsalvo assisted with the experiments. J.H. Lienhard conducted the technical analysis and supervised the project. The manuscript was prepared and reviewed by all authors.

Declaration of Competing Interest

The authors declare no competing financial or personal conflicts of interest that would have appeared to influence the content of this paper.

References

(1) Alkhadra, M. A.; Su, X.; Suss, M. E.; Tian, H.; Guyes, E. N.; Shocron, A. N.; Conforti, K. M.; Pedro De Souza, J.; Kim, N.; Tedesco, M.; Khoiruddin, K.; Wenten, G.; Santiago, J. G.; Hatton, T. A.; Bazant, M. Z. Electrochemical Methods for Water Purification, Ion Separations, and Energy Conversion. *Chemical Reviews* **2022**, *122*, 13547–13635.

(2) Epsztein, R.; DuChanois, R. M.; Ritt, C. L.; Noy, A.; Elimelech, M. Towards single-species selectivity of membranes with subnanometre pores. *Nature Nanotechnology* **2020**, *15*, 426–436.

(3) Kumar, A.; Kim, Y.; Su, X.; Fukuda, H.; Naidu, G.; Du, F.; Vigneswaran, S.; Drioli, E.; Hatton, T. A.; Lienhard, J. H. Advances and challenges in metal ion separation from water. *Trends in Chemistry* **2021**, *3*, 819–831.

(4) Khalil, A.; Mohammed, S.; Hashaikeh, R.; Hilal, N. Lithium recovery from brine: Recent developments and challenges. *Desalination* **2022**, *528*, 115611.

23

(5) Kumar, A.; Naidu, G.; Fukuda, H.; Du, F.; Vigneswaran, S.; Drioli, E.; Lienhard, J. H. Metals Recovery from Seawater Desalination Brines: Technologies, Opportunities, and Challenges. *ACS Sustainable Chemistry & Engineering* **2021**, *9*, 7704–7712.

(6) Wu, L.; Zhang, C.; Kim, S.; Hatton, T. A.; Mo, H.; David Waite, T. Lithium recovery using electrochemical technologies: Advances and challenges. *Water Research* **2022**, *221*, 118822.

(7) Meshram, P.; Pandey, B. D.; Mankhand, T. R. Extraction of lithium from primary and secondary sources by pre-treatment, leaching and separation: A comprehensive review. *Hydrometallurgy* **2014**, *150*, 192–208.

(8) Yang, S.; Zhang, F.; Ding, H.; He, P.; Zhou, H. Lithium Metal Extraction from Seawater. *Joule* **2018**, *2*, 1648–1651.

(9) Foo, Z. H.; Stetson, C.; Dach, E.; Deshmukh, A.; Lee, H.; Menon, A.; Prasher, R.; Lienhard, J. H.; Wilson, A. D. Solvent-driven aqueous separations for hypersaline brine concentration and resource recovery. *Trends in Chemistry* **2022**, *4*, 1078–1093.

(10) Boo, C.; Billinge, I. H.; Chen, X.; Shah, K. M.; Yip, N. Y. Zero Liquid Discharge of Ultrahigh-Salinity Brines with Temperature Swing Solvent Extraction. *Environmental Science and Technology* **2020**, *54*, 9124–9131.

(11) Li, H.; Wang, Y.; Li, T.; Ren, X.-k.; Wang, J.; Wang, Z.; Zhao, S. Nanofiltration Membrane with Crown Ether as Exclusive Li+ Transport Channels Achieving Efficient Extraction of Lithium from Salt Lake Brine. *Chemical Engineering Journal* **2022**, *438*, 135658.

(12) Pavluchkov, V.; Shefer, I.; Peer-Haim, O.; Blotevogel, J.; Epsztein, R. Indications of ion dehydration in diffusion-only and pressure-driven nanofiltration. *Journal of Membrane Science* **2022**, *648*, 120358.

(13) Qiu, Y.; Ruan, H.; Tang, C.; Yao, L.; Shen, J.; Sotto, A. Study on recovering high-concentration lithium salt from lithium-containing wastewater using a hybrid reverse osmosis (RO)-electrodialysis (ED) process. *ACS Sustainable Chemistry & Engineering* **2019**, *7*, 13481–13490.

(14) Chen, Q. B.; Ji, Z. Y.; Liu, J.; Zhao, Y. Y.; Wang, S. Z.; Yuan, J. S. Development of recovering lithium from brines by selective-electrodialysis: Effect of coexisting cations on the migration of lithium. *Journal of Membrane Science* **2018**, *548*, 408–420.

(15) Fan, H.; Yip, N. Y. Elucidating conductivity-permselectivity tradeoffs in electrodialysis and reverse electrodialysis by structure-property analysis of ion-exchange membranes. *Journal of Membrane Science* **2019**, *573*, 668–681.

(16) Wang, H.; Jones, L. O.; Hwang, I.; Allen, M. J.; Tao, D.; Lynch, V. M.; Freeman, B. D.; Khashab, N. M.; Schatz, G. C.; Page, Z. A.; Sessler, J. L. Selective Separation of Lithium Chloride by Organogels Containing Strapped Calix[4]pyrroles. *Journal of the American Chemical Society* **2021**, *143*, 20403–20410.

(17) Sachar, H. S.; Zofchak, E. S.; Marioni, N.; Zhang, Z.; Kadulkar, S.; Duncan, T. J.; Freeman, B. D.; Ganesan, V. Impact of Cation-Ligand Interactions on the Permselectivity of Ligand-Functionalized Polymer Membranes in Single and Mixed Salt Systems. *Macromolecules* **2022**, *55*, 4821–4831.

(18) Park, S. H.; Kim, J. H.; Moon, S. J.; Jung, J. T.; Wang, H. H.; Ali, A.; Quist-Jensen, C. A.; Macedonio, F.; Drioli, E.; Lee, Y. M. Lithium recovery from artificial brine using energy-efficient membrane distillation and nanofiltration. *Journal of Membrane Science* **2020**, *598*, 117683.

(19) Nie, X. Y.; Sun, S. Y.; Sun, Z.; Song, X.; Yu, J. G. Ion-fractionation of lithium ions from magnesium ions by electrodialysis using monovalent selective ion-exchange membranes. *Desalination* **2017**, *403*, 128–135.

(20) Wang, R.; Lin, S. Pore model for nanofiltration: History, theoretical framework, key predictions, limitations, and prospects. *Journal of Membrane Science* **2021**, *620*.

(21) Luo, J.; Wan, Y. Effects of pH and salt on nanofiltration-a critical review. *Journal of Membrane Science* **2013**, *438*, 18–28.

(22) Zhao, Y.; Tong, T.; Wang, X.; Lin, S.; Reid, E. M.; Chen, Y. Differentiating Solutes with Precise Nanofiltration for Next Generation Environmental Separations: A Review. *Environmental Science and Technology* **2021**, *55*, 1359–1376.

(23) Shefer, I.; Lopez, K.; Straub, A. P.; Epsztein, R. Applying Transition-State Theory to Explore Transport and Selectivity in Salt-Rejecting Membranes: A Critical Review. *Environmental Science and Technology* **2022**, *14*, 11.

(24) Wang, X.; Fang, D.; Hsiao, B. S.; Chu, B. Nanofiltration membranes based on thin-film nanofibrous composites. *Journal of Membrane Science* **2014**, *469*, 188–197.

(25) Ritt, C. L.; Werber, J. R.; Wang, M.; Yang, Z.; Zhao, Y.; Kulik, H. J.; Elimelech, M. Ionization behavior of nanoporous polyamide membranes. *Proceedings of the National Academy of Sciences of the United States of America* **2020**, *117*, 30191–30200.

(26) Heiranian, M.; Duchanois, R. M.; Ritt, C. L.; Violet, C.; Elimelech, M. Molecular Simulations to Elucidate Transport Phenomena in Polymeric Membranes. *Environmental Science and Technology* **2022**, *56*, 3313–3323.

(27) Epsztein, R.; Shaulsky, E.; Dizge, N.; Warsinger, D. M.; Elimelech, M. Role of Ionic Charge Density in Donnan Exclusion of Monovalent Anions by Nanofiltration. *Environmental Science and Technology* **2018**, *52*, 4108–4116.

(28) Labban, O.; Liu, C.; Chong, T. H.; Lienhard, J. H. Fundamentals of low-pressure nanofiltration: Membrane characterization, modeling, and understanding the multi-ionic interactions in water softening. *Journal of Membrane Science* **2017**, *521*, 18–32.

26

(29) Yaroshchuk, A.; Bruening, M. L.; Zholkovskiy, E. Modelling nanofiltration of electrolyte solutions. *Advances in Colloid and Interface Science* **2019**, *268*, 39–63.

(30) Lu, C.; Hu, C.; Ritt, C. L.; Hua, X.; Sun, J.; Xia, H.; Liu, Y.; Li, D. W.; Ma, B.; Elimelech, M.; Qu, J. In Situ Characterization of Dehydration during Ion Transport in Polymeric Nanochannels. *Journal of the American Chemical Society* **2021**, *143*, 14242–14252.

(31) Stolov, M.; Freger, V. Membrane Charge Weakly Affects Ion Transport in Reverse Osmosis. *Environmental Science & Technology Letters* **2020**, *7*, 440–445.

(32) Aydogan Gokturk, P.; Sujanani, R.; Qian, J.; Wang, Y.; Katz, L. E.; Freeman, B. D.; Crumlin, E. J. The Donnan potential revealed. *Nature Communications* **2022**, *13*, 1–7.

(33) Léniz-Pizarro, F.; Liu, C.; Colburn, A.; Escobar, I. C.; Bhattacharyya, D. Positively charged nanofiltration membrane synthesis, transport models, and lanthanides separation. *Journal of Membrane Science* **2021**, *620*, 118973.

(34) Wang, L.; Rehman, D.; Sun, P. F.; Deshmukh, A.; Zhang, L.; Han, Q.; Yang, Z.; Wang, Z.; Park, H. D.; Lienhard, J. H.; Tang, C. Y. Novel Positively Charged Metal-Coordinated Nanofiltration Membrane for Lithium Recovery. *ACS Applied Materials and Interfaces* **2021**, *13*, 16906–16915.

(35) Gu, T.; Zhang, R.; Zhang, S.; Shi, B.; Zhao, J.; Wang, Z.; Long, M.; Wang, G.; Qiu, T.; Jiang, Z. Quaternary ammonium engineered polyamide membrane with high positive charge density for efficient Li + /Mg 2+ separation. *Journal of Membrane Science* **2022**, *659*, 120802.

(36) Guo, C.; Li, N.; Qian, X.; Shi, J.; Jing, M.; Teng, K.; Xu, Z. Ultra-thin double Janus nanofiltration membrane for separation of Li + and Mg 2+ : "Drag" effect from carboxyl-containing negative interlayer-thin Double Janus NF membrane Hydropho-

27

bic/hydrophilic Positive/negative charge Separation of Li + and Mg 2+. *Separation and Purification Technology* **2020**, *230*, 115567.

(37) Zhang, H. Z.; Xu, Z. L.; Ding, H.; Tang, Y. J. Positively charged capillary nanofiltration membrane with high rejection for Mg2 + and Ca2 + and good separation for Mg2 + and Li +. *Desalination* **2017**, *420*, 158–166.

(38) Razmjou, A.; Asadnia, M.; Hosseini, E.; Habibnejad Korayem, A.; Chen, V. Design principles of ion selective nanostructured membranes for the extraction of lithium ions. *Nature Communications* **2019**, *10*, 1–15.

(39) Sujanani, R.; Landsman, M. R.; Jiao, S.; Moon, J. D.; Shell, M. S.; Lawler, D. F.; Katz, L. E.; Freeman, B. D. Designing Solute-Tailored Selectivity in Membranes: Perspectives for Water Reuse and Resource Recovery. *ACS Macro Letters* **2020**, *9*, 1709–1717.

(40) Košutić, K.; Dolar, D.; Kunst, B. On experimental parameters characterizing the reverse osmosis and nanofiltration membranes' active layer. *Journal of Membrane Science* **2006**, *282*, 109–114.

(41) Xu, P.; Wang, W.; Qian, X.; Wang, H.; Guo, C.; Li, N.; Xu, Z.; Teng, K.; Wang, Z. Positive charged PEI-TMC composite nanofiltration membrane for separation of Li+ and Mg2+ from brine with high Mg2+/Li+ ratio. *Desalination* **2019**, *449*, 57–68.

(42) Li, Y.; Wang, S.; Wu, W.; Yu, H.; Che, R.; Kang, G.; Cao, Y. Fabrication of positively charged nanofiltration membrane with uniform charge distribution by reversed interfacial polymerization for Mg 2+ / Li + separation. *Journal of Membrane Science* **2022**, *659*, 120809.

(43) Pramanik, B. K.; Asif, M. B.; Roychand, R.; Shu, L.; Jegatheesan, V.; Bhuiyan, M.; Hai, F. I. Lithium recovery from salt-lake brine: Impact of competing cations, pretreatment and preconcentration. *Chemosphere* **2020**, *260*.

(44) Zhai, X.; Wang, Y.-L.; Dai, R.; Li, X.; Wang, Z. Roles of AnionCation Coupling Transport and Dehydration-Induced IonMembrane Interaction in Precise Separation of Ions by Nanofiltration Membranes. *Environmental Science and Technology* **2022**, *56*, 14069–14079.

(45) Williams, A. E.; McKibben, M. A. A brine interface in the Salton Sea Geothermal System, California: Fluid geochemical and isotopic characteristics. *Geochimica et Cosmochimica Acta* **1989**, *53*, 1905–1920.

(46) Goon, G. S.; Labban, O.; Foo, Z. H.; Zhao, X.; Lienhard, J. H. Deformation-induced cleaning of organically fouled membranes: Fundamentals and techno-economic assessment for spiral-wound membranes. *Journal of Membrane Science* **2021**, *626*, 119169.

(47) Geraldes, V.; Brites Alves, A. M. Computer program for simulation of mass transport in nanofiltration membranes. *Journal of Membrane Science* **2008**, *321*, 172–182.

(48) Liang, Y.; Zhu, Y.; Liu, C.; Lee, K. R.; Hung, W. S.; Wang, Z.; Li, Y.; Elimelech, M.; Jin, J.; Lin, S. Polyamide nanofiltration membrane with highly uniform sub-nanometre pores for sub-1 Å precision separation. *Nature Communications* **2020**, *11*, 2015.

(49) Labban, O.; Liu, C.; Chong, T. H.; Lienhard, J. H. Relating transport modeling to nanofiltration membrane fabrication: Navigating the permeability-selectivity trade-off in desalination pretreatment. *Journal of Membrane Science* **2018**, *554*, 26–38.

(50) Yaroshchuk, A.; Bruening, M. L.; Licón Bernal, E. E. Solution-Diffusion-Electro-Migration model and its uses for analysis of nanofiltration, pressure-retarded osmosis and forward osmosis in multi-ionic solutions. *Journal of Membrane Science* **2013**, *447*, 463–476.

(51) Duignan, T. T.; Zhao, X. S. The Born model can accurately describe electrostatic ion solvation. *Physical Chemistry Chemical Physics* **2020**, *22*, 25126–25135.

(52) Mohammad, A. W.; Hilal, N.; Al-Zoubi, H.; Darwish, N. A. Prediction of permeate fluxes and rejections of highly concentrated salts in nanofiltration membranes. *Journal of Membrane Science* **2007**, *289*, 40–50.

(53) Taylor, R.; Krishna, R. *Multicomponent mass transfer*; Wiley, 1993; p 579.

(54) Oren, Y. S.; Freger, V.; Nir, O. New compact expressions for concentration-polarization of trace-ions in pressure-driven membrane processes. *Journal of Membrane Science Letters* **2021**, *1*, 100003.

(55) Tow, E. W.; Lienhard, J. H. Quantifying osmotic membrane fouling to enable comparisons across diverse processes. *Journal of Membrane Science* **2016**, *511*, 92–107.

(56) Rehman, D.; Lienhard, J. H. Global optimization for accurate and efficient parameter estimation in nanofiltration. *Journal of Membrane Science Letters* **2022**, 100034.

(57) Micari, M.; Diamantidou, D.; Heijman, B.; Moser, M.; Haidari, A.; Spanjers, H.; Bertsch, V. Experimental and theoretical characterization of commercial nanofiltration membranes for the treatment of ion exchange spent regenerant. *Journal of Membrane Science* **2020**, *606*, 118117.

(58) Marcus, Y.; Hefter, G. Ion pairing. *Chemical Reviews* **2006**, *106*, 4585–4621.

(59) Wilson, A. D.; Lee, H.; Stetson, C. Mass action model of solution activity via speciation by solvation and ion pairing equilibria. *Communications Chemistry* **2021**, *4*, 1–8.

(60) Foo, Z. H.; Rehman, D.; Coombs, O. Z.; Deshmukh, A.; Lienhard, J. H. Multicomponent Fickian solution-diffusion model for osmotic transport through membranes. *Journal of Membrane Science* **2021**, *640*, 119819.

(61) Lu, X.; Boo, C.; Ma, J.; Elimelech, M. Bidirectional diffusion of ammonium and sodium cations in forward osmosis: Role of membrane active layer surface chemistry and charge. *Environmental Science and Technology* **2014**, *48*, 14369–14376.

(62) Oatley, D. L.; Llenas, L.; Pérez, R.; Williams, P. M.; Martínez-Lladó, X.; Rovira, M. Review of the dielectric properties of nanofiltration membranes and verification of the single oriented layer approximation. *Advances in Colloid and Interface Science* **2012**, *173*, 1–11.

(63) Lin, Y. L.; Chiang, P. C.; Chang, E. E. Removal of small trihalomethane precursors from aqueous solution by nanofiltration. *Journal of Hazardous Materials* **2007**, *146*, 20–29.

(64) Dalwani, M.; Benes, N. E.; Bargeman, G.; Stamatialis, D.; Wessling, M. Effect of pH on the performance of polyamide/polyacrylonitrile based thin film composite membranes. *Journal of Membrane Science* **2011**, *372*, 228–238.

(65) Sutariya, B.; Karan, S. A realistic approach for determining the pore size distribution of nanofiltration membranes. *Separation and Purification Technology* **2022**, *293*, 1383–5866.

(66) Wang, J.; Armstrong, M. D.; Grzebyk, K.; Vickers, R.; Coronell, O. Effect of Feed Water pH on the Partitioning of Alkali Metal Salts from Aqueous Phase into the Polyamide Active Layers of Reverse Osmosis Membranes. *Environmental Science and Technology* **2021**, *55*, 3250–3259.

(67) Marcus, Y. The solvation number of ions obtained from their entropies of solvation. *Journal of Solution Chemistry* **1986**, *15*, 291–306.

(68) Ritt, C. L.; Pedro De Souza, J.; Barsukov, M. G.; Yosinski, S.; Bazant, M. Z.; Reed, M. A.; Elimelech, M. Thermodynamics of Charge Regulation during Ion Transport through Silica Nanochannels. *ACS Nano* **2022**, *16*, 15249–15260.

(69) Liu, S.; Ganti-Agrawal, S.; Keten, S.; Lueptow, R. M. Molecular insights into charged nanofiltration membranes: Structure, water transport, and water diffusion. *Journal of Membrane Science* **2022**, *644*, 120057.

(70) Zhang, H.; He, Q.; Luo, J.; Wan, Y.; Darling, S. B. Sharpening Nanofiltration: Strategies for Enhanced Membrane Selectivity. *ACS Applied Materials and Interfaces* **2020**, *12*, 39948–39966.

(71) Chan, E. P.; Frieberg, B. R.; Ito, K.; Tarver, J.; Tyagi, M.; Zhang, W.; Coughlin, E. B.; Stafford, C. M.; Roy, A.; Rosenberg, S.; Soles, C. L. Insights into the Water Transport Mechanism in Polymeric Membranes from Neutron Scattering. *Macromolecules* **2020**, *53*, 1443–1450.

(72) Wilson, A. D.; Lee, H.; Stetson, C. Local stress within a granular molecular solvent matrix, a mechanism for individual ion hydration. *Journal of Molecular Liquids* **2022**, 119544.

(73) Zhou, X.; Wang, Z.; Epsztein, R.; Zhan, C.; Li, W.; Fortner, J. D.; Pham, T. A.; Kim, J. H.; Elimelech, M. Intrapore energy barriers govern ion transport and selectivity of desalination membranes. *Science Advances* **2020**, *6*.

(74) Malmir, H.; Epsztein, R.; Elimelech, M.; Haji-Akbari, A. Induced Charge Anisotropy: A Hidden Variable Affecting Ion Transport through Membranes. *Matter* **2020**, *2*, 735–750.

(75) Kingsbury, R. S.; Wang, J.; Coronell, O. Comparison of water and salt transport properties of ion exchange, reverse osmosis, and nanofiltration membranes for desalination and energy applications. *Journal of Membrane Science* **2020**, *604*, 117998.

(76) Pedro De Souza, J.; Chow, C.-M.; Karnik, R.; Bazant, M. Z. Nonlinear ion transport mediated by induced charge in ultrathin nanoporous membranes. *Physical Review E* **2021**, *104*, 44802.

(77) Ranjan Puhan, M.; Sutariya, B.; Karan, S. Revisiting the alkali hydrolysis of polyamide nanofiltration membranes. *Journal of Membrane Science* **2022**, *661*, 120887.

(78) Ibrahim, Y.; Wadi, V. S.; Ouda, M.; Naddeo, V.; Banat, F.; Hasan, S. W. Highly selective heavy metal ions membranes combining sulfonated polyethersulfone and self-assembled manganese oxide nanosheets on positively functionalized graphene oxide nanosheets. *Chemical Engineering Journal* **2022**, *428*, 131267.

TOC Graphic
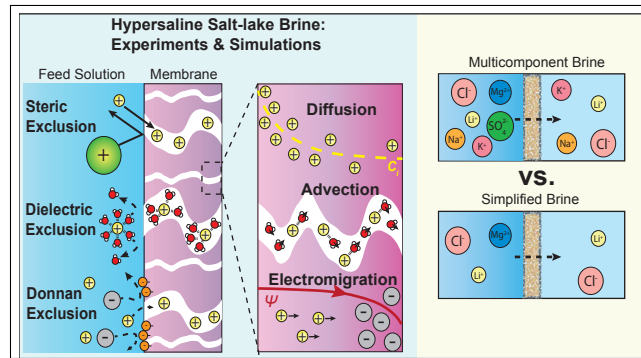
Supporting Information

Lithium Concentration from Salt-lake Brine

by Donnan-enhanced Nanofiltration

4   Zi Hao Foo,[†,‡] Danyal Rehman,[†,‡] Andrew T. Bouma,[†] Sebastian Monsalvo,[†] and

5   John H. Lienhard[*,†]

6   †*Department of Mechanical Engineering, Massachusetts Institute of Technology,*

7   *Cambridge, Massachusetts 02139, United States*

8   ‡*Center for Computational Science and Engineering, Massachusetts Institute of*

9   *Technology, Cambridge, Massachusetts 02139, United States*

E-mail: lienhard@mit.edu

10

11   Number of Pages: 40. Number of Figures: 10. Number of Tables: 12.

Contents

List of Figures

List of Tables

A Experimental Methods

A.1 Volume Calibration

The flow loop volume of the experimental apparatus is calibrated to accurately represent the solution concentrations (Fig. 1A in the main text).[6] First, deionized (DI) water is introduced into the flow loop, without retentate recycling, until the conductivity of the retentate falls within 1 % of the DI water. Next, an NaCl feed solution with a pre-determined initial concentration is passed through the flow loop and recycled until the conductivity of the solution reaches a steady state. The initial and final concentrations of the NaCl solutions are determined with ICP-OES, and are plotted in Supp. Fig. 1A. Linear regression is performed to elucidate the volume of the flow loop, based on Eq. 1.

$$C_{NaCl,f} = C_{NaCl,0} \left(\frac{V_{Solution}}{V_{Solution} + V_{Loop}} \right)$$ (1)

where $C_{NaCl,0}$ and $C_{NaCl,f}$ denote the initial and final measured NaCl concentrations, and $V_{Solution}$ and V_{Loop} denote the volume of the solution tank and flow loop, respectively.
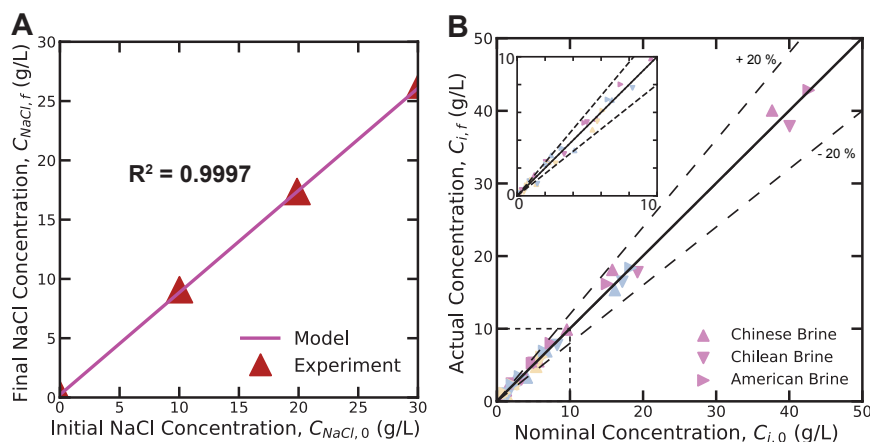
Supplementary Figure 1: **A**) Plot of the final feed NaCl concentration against the initial feed NaCl concentration, following dilution of the feed from the water in the flow loops of the nanofiltration experimental apparatus. **B**) Plot of the nominal species concentrations (by design) against the actual species concentrations (from ICP-OES). The maximum deviation for the concentration of the species is 18.5 %.

The derived flow loop volume is incorporated to prepare the feed solutions for all the experiments. A comparison between the nominal and actual concentrations of the inorganic solutes in the respective brines is presented in Supp. Fig. 1B. The maximum absolute deviation in the species concentrations is 18.5 %.

A.2 Multicomponent Salt-lake Brine

Synthetic multicomponent brine is prepared based on the aqueous composition of the salt-lakes in Salar de Atacama,[3] Qaidam Lake,[4] and Salton Sea.[5] Diluted variants of the respective brine, as provided in Supp.Table 1, 2 and 3, are prepared while keeping the relative ionic ratios constant. The total dissolved solids (TDS) concentrations of the experimental solutions are 10, 30, 70, 150 and 250 g/L.

Supplementary Table 1: Nominal ionic composition of feed solution based on brine from Salar de Atacama,[3] at total dissolved concentrations of 10, 30, 70, 150 and 250 g/L.

Salt Lake, Location	Nominal Composition (g/L)							
	Li^+	Na^+	K^+	Mg^{2+}	Ca^{2+}	Cl^-	SO_4^{2-}	TDS
Salar de Atacama, Chile	1.19	69.01	17.89	7.31	—	143.72	12.06	251.18
	0.71	41.21	10.68	4.37	—	85.83	7.20	150.00
	0.33	19.23	4.99	2.04	—	40.10	3.36	70.00
	0.14	8.24	2.14	0.87	—	17.17	1.44	30.00
	0.05	2.75	0.71	0.29	—	5.72	0.48	10.00

Supplementary Table 2: Nominal ionic composition of feed solution based on brine from Qaidam Lake,[4] at total dissolved concentrations of 10, 30, 70, 150 and 250 g/L.

Salt Lake, Location	Nominal Composition (g/L)							
	Li^+	Na^+	K^+	Mg^{2+}	Ca^{2+}	Cl^-	SO_4^{2-}	TDS
Qaidam Lake, China	0.31	56.30	4.40	20.20	—	134.20	34.10	249.51
	0.19	33.85	2.65	12.14	—	80.68	20.50	150.00
	0.09	15.79	1.23	5.67	—	37.65	9.57	70.00
	0.04	6.77	0.53	2.43	—	16.14	4.10	30.00
	0.01	2.26	0.18	0.81	—	5.38	1.37	10.00

Supplementary Table 3: Nominal ionic composition of feed solution based on brine from Salton Sea,[5] at total dissolved concentrations of 10, 30, 70, 150 and 250 g/L.

Salt Lake, Location	Nominal Composition (g/L)							
	Li^+	Na^+	K^+	Mg^{2+}	Ca^{2+}	Cl^-	SO_4^{2-}	TDS
	0.22	53.70	17.10	—	26.30	152.00	0.12	249.44
	0.13	32.29	10.28	—	15.82	91.40	0.07	150.00
Salton Sea, United States	0.06	15.07	4.80	—	7.38	42.66	0.03	70.00
	0.03	6.46	2.06	—	3.16	18.28	0.01	30.00
	0.01	2.15	0.69	—	1.05	6.09	< 0.01	10.00

Nanofiltration experiments are conducted based on the description provided in the *Materials and Methods* section of the main text. The ionic compositions are analyzed based on inductively coupled plasma optical emission spectroscopy (ICP-OES), using a three point calibration standard based on standard solutions from MilliporeSigma (Trace-Cert). The chosen wavelengths for spectroscopic analysis are given in Supp.Table 4. The maximum uncertainty in each concentration measurement is less than 2 %.

A detailed breakdown of the experimental conditions, including the feed temperature, concentration, pressure and solution pH, and the corresponding rejection results, are provided in Supp.Table 5, 6, 7. From these measurements, the separation factors between Li^+ and Mg^{2+}, and between Cl^- and SO_4^{2-}, are calculated and plotted against the solution concentrations in Supp. Fig. 2A - E. Analysis of the Cl^- and SO_4^{2-} separation with Salton Sea brine is not provided as the concentrations of sulfate ions in the permeate solution are under the detection limits of ICP-OES.

Supplementary Table 4: Selected wavelengths for spectroscopic analysis with ICP-OES.

Elements	ICP-OES wavelength (nm)
Na	568.263
K	404.721
Li	323.263
Mg	277.983
Ca	373.690
Cl	774.497
S	180.669

Supplementary Table 5: Experimental measurements for NF 270 based on brine from Salar de Atacama,[3] at solution pH of 7 and 2, and total dissolved concentrations of 10, 30, 70, 150 and 250 g/L.

Nominal Feed Salinity (g/L)	Feed pH (-)	Feed Pressure (bar)	Temperature (°C)	Water Flux (LMH)	Species Rejection (-)						
					Li^+	Na^+	K^+	Mg^{2+}	Ca^{2+}	Cl^-	SO_4^{2-}
10	6.85	2.5	20.0	14.89	0.051	0.067	0.059	0.477	—	0.067	0.971
10	6.85	4	20.0	26.32	0.061	0.090	0.071	0.545	—	0.101	0.975
10	6.89	6	20.0	44.44	0.093	0.139	0.090	0.608	—	0.143	0.974
10	6.89	10	20.0	78.15	0.126	0.192	0.119	0.651	—	0.171	0.974
10	2.11	2.5	20.0	10.41	0.034	0.035	0.031	0.861	—	0.142	0.677
10	2.12	4	20.0	17.66	0.047	0.054	0.060	0.960	—	0.148	0.638
10	2.13	6	20.0	30.90	0.123	0.145	0.130	0.968	—	0.217	0.728
10	2.13	10	20.0	60.41	0.227	0.266	0.231	0.972	—	0.302	0.818
30	6.95	4	20.0	18.05	0.037	0.061	0.041	0.516	—	0.051	0.972
30	7.01	8	20.0	42.01	0.088	0.131	0.088	0.631	—	0.118	0.979
30	6.96	12	20.0	68.40	0.094	0.147	0.072	0.649	—	0.119	0.975
30	6.93	16	20.0	88.54	0.104	0.160	0.089	0.661	—	0.129	0.974
30	2.14	4	20.0	11.11	0.008	0.006	0.002	0.868	—	0.098	0.743
30	2.15	8	20.0	30.21	0.094	0.111	0.100	0.958	—	0.176	0.828
30	2.15	12	20.0	48.95	0.154	0.182	0.142	0.964	—	0.248	0.878
30	2.16	16	20.0	67.36	0.193	0.230	0.182	0.966	—	0.267	0.902
70	6.93	8	20.0	25.69	0.012	0.015	-0.006	0.530	—	0.046	0.968
70	7.06	12	20.0	41.57	0.027	0.034	0.001	0.592	—	0.088	0.975
70	7.26	16	20.0	55.55	0.055	0.077	0.037	0.623	—	0.108	0.973
70	7.41	24	20.0	77.77	0.058	0.091	0.031	0.610	—	0.094	0.971
70	2.06	8	20.0	15.13	-0.041	-0.027	-0.053	0.879	—	0.069	0.814
70	2.06	12	20.0	28.40	0.004	0.026	-0.028	0.928	—	0.101	0.876
70	2.07	16	20.0	39.23	0.046	0.082	0.009	0.938	—	0.134	0.902
70	2.08	24	20.0	63.54	0.103	0.153	0.062	0.946	—	0.175	0.931
150	7.26	12	20.0	17.70	0.032	0.072	0.002	0.519	—	0.053	0.966
150	7.27	18	20.0	28.75	0.019	0.052	-0.025	0.579	—	0.046	0.974
150	7.20	24	20.0	40.60	0.048	0.106	0.005	0.618	—	0.082	0.976
150	7.28	32	20.0	55.42	0.074	0.124	0.011	0.637	—	0.102	0.977
150	1.91	12	20.0	13.13	-0.061	-0.068	-0.095	0.806	—	0.008	0.844
150	1.92	18	20.0	23.26	-0.033	-0.024	-0.093	0.877	—	0.060	0.903
150	1.93	24	20.0	32.63	-0.012	0.012	-0.073	0.900	—	0.070	0.925
150	1.93	32	20.0	44.34	0.032	0.078	-0.034	0.917	—	0.114	0.945
250	7.11	24	20.0	22.80	-0.031	-0.036	-0.090	0.486	—	-0.008	0.953
250	7.19	28	20.0	28.06	-0.022	0.006	-0.092	0.525	—	-0.006	0.967
250	7.12	32	20.0	32.29	-0.010	0.008	-0.086	0.543	—	0.012	0.967
250	7.17	36	20.0	36.02	0.014	0.051	-0.057	0.563	—	0.035	0.971
250	1.84	24	20.0	21.57	-0.069	-0.067	-0.143	0.721	—	0.017	0.916
250	1.87	28	20.0	24.30	-0.054	-0.061	-0.142	0.792	—	0.043	0.934
250	1.88	32	20.0	27.40	-0.027	0.009	-0.113	0.812	—	0.056	0.941
250	1.89	36	20.0	30.90	0.392	0.026	-0.111	0.826	—	0.059	0.950

Supplementary Table 6: Experimental measurements for NF 270 based on brine from Qaidam Lake, [4] at solution pH of 7 and 2, and total dissolved concentrations of 10, 30, 70, 150 and 250 g/L.

| Nominal Feed Salinity (g/L)	Feed pH (-)	Feed Pressure (bar)	Temperature (°C)	Water Flux (LMH)	Species Rejection (-)						
					Li^+	Na^+	K^+	Mg^{2+}	Ca^{2+}	Cl^-	SO_4^{2-}
10	7.02	2.5	20.0	14.54	0.026	-0.018	0.017	0.457	—	0.047	0.974
10	7.41	4	20.0	28.75	0.066	0.064	0.056	0.546	—	0.121	0.982
10	7.40	6	20.0	44.40	0.096	0.100	0.086	0.599	—	0.181	0.981
10	7.32	10	20.0	82.63	0.129	0.154	0.106	0.656	—	0.227	0.979
10	2.07	2.5	20.0	7.63	-0.070	-0.078	-0.057	0.909	—	0.230	0.669
10	2.08	4	20.0	17.66	0.038	0.018	0.060	0.971	—	0.306	0.720
10	2.08	6	20.0	32.63	0.173	0.150	0.194	0.977	—	0.401	0.800
10	2.09	10	20.0	64.78	0.314	0.324	0.331	0.981	—	0.484	0.872
30	7.31	4	20.0	10.41	0.033	0.046	0.023	0.521	—	0.073	0.950
30	7.26	8	20.0	32.49	0.044	0.040	0.033	0.657	—	0.146	0.971
30	7.30	12	20.0	50.00	0.063	0.065	0.059	0.696	—	0.188	0.971
30	7.31	16	20.0	68.40	0.069	0.078	0.060	0.719	—	0.204	0.973
30	2.05	4	20.0	5.90	-0.112	-0.107	-0.117	0.865	—	0.194	0.576
30	2.01	8	20.0	20.13	-0.028	-0.037	-0.019	0.956	—	0.280	0.730
30	2.03	12	20.0	36.02	0.063	0.071	0.056	0.969	—	0.332	0.823
30	2.06	16	20.0	53.13	0.152	0.163	0.153	0.975	—	0.400	0.874
70	7.27	8	20.0	8.68	-0.019	-0.026	-0.047	0.535	—	0.067	0.944
70	6.87	12	20.0	18.75	-0.004	0.005	-0.067	0.646	—	0.133	0.966
70	7.00	16	20.0	28.40	-0.005	0.006	-0.062	0.692	—	0.141	0.968
70	7.06	24	20.0	46.57	0.034	0.047	-0.017	0.740	—	0.183	0.975
70	2.03	8	20.0	4.17	-0.088	-0.060	-0.140	0.693	—	0.112	0.715
70	2.03	12	20.0	11.80	-0.114	-0.073	-0.155	0.896	—	0.182	0.819
70	2.07	16	20.0	20.78	-0.060	-0.029	-0.114	0.931	—	0.210	0.883
70	2.05	24	20.0	38.54	0.004	0.047	-0.059	0.955	—	0.259	0.933
150	7.16	18	20.0	10.06	-0.070	-0.029	-0.129	0.573	—	0.033	0.905
150	7.25	24	20.0	15.63	-0.081	-0.037	-0.160	0.642	—	0.057	0.941
150	7.30	32	20.0	24.24	-0.100	-0.044	-0.192	0.689	—	0.038	0.945
150	7.31	38	20.0	30.20	-0.072	-0.024	-0.173	0.709	—	0.092	0.951
150	2.12	18	20.0	6.94	-0.178	-0.149	-0.252	0.744	—	0.075	0.724
150	2.12	24	20.0	11.96	-0.146	-0.098	-0.228	0.839	—	0.139	0.833
150	2.07	32	20.0	20.64	-0.142	-0.081	-0.252	0.890	—	0.148	0.893
150	2.07	38	20.0	25.00	-0.123	-0.063	-0.229	0.903	—	0.163	0.913
250	7.12	28	20.0	7.97	-0.060	-0.002	-0.141	0.548	—	0.021	0.891
250	7.28	32	20.0	10.04	-0.068	-0.014	-0.140	0.587	—	0.033	0.914
250	7.17	36	20.0	12.15	-0.232	-0.202	-0.343	0.552	—	-0.100	0.904
250	7.20	40	20.0	13.89	-0.080	-0.028	-0.177	0.632	—	0.054	0.928
250	1.93	28	20.0	7.62	-0.135	-0.070	-0.214	0.634	—	0.006	0.827
250	1.96	32	20.0	9.38	-0.176	-0.104	-0.270	0.704	—	0.027	0.853
250	1.99	36	20.0	10.76	-0.206	-0.147	-0.330	0.740	—	0.009	0.867
250	2.01	40	20.0	12.84	-0.214	-0.147	-0.324	0.772	—	0.012	0.896

Supplementary Table 7: Experimental measurements for NF 270 based on brine from Salton Sea,[5] at solution pH of 7 and 2, and total dissolved concentrations of 10, 30, 70, 150 and 250 g/L.

Nominal Feed Salinity (g/L)	Feed pH (-)	Feed Pressure (bar)	Temperature (°C)	Water Flux (LMH)	Species Rejection (-)						
					Li^+	Na^+	K^+	Mg^{2+}	Ca^{2+}	Cl^-	SO_4^{2-}
10	6.94	2.5	20.0	31.40	0.032	0.031	0.024	—	0.322	0.130	—
10	7.00	4	20.0	46.88	0.053	0.038	0.050	—	0.373	0.139	—
10	6.99	8	20.0	98.26	0.081	0.028	0.080	—	0.443	0.220	—
10	6.98	10	20.0	114.93	0.069	0.055	0.063	—	0.449	0.231	—
10	1.96	2.5	20.0	13.54	-0.005	-0.005	-0.057	—	0.806	0.276	—
10	1.95	4	20.0	24.65	0.112	0.112	0.097	—	0.927	0.355	—
10	1.96	8	20.0	59.72	0.278	0.278	0.272	—	0.940	0.443	—
10	1.96	10	20.0	74.30	0.307	0.307	0.294	—	0.935	0.450	—
30	6.85	4	20.0	21.52	-0.013	-0.181	-0.050	—	0.375	0.146	—
30	6.84	8	20.0	47.22	0.000	-0.434	-0.042	—	0.459	0.174	—
30	6.83	12	20.0	70.48	0.025	0.126	-0.013	—	0.485	0.217	—
30	6.81	16	20.0	94.79	0.048	0.280	0.006	—	0.486	0.244	—
30	2.03	4	20.0	9.375	-0.122	-0.382	-0.157	—	0.708	0.199	—
30	2.02	8	20.0	28.12	-0.033	0.156	-0.043	—	0.868	0.319	—
30	2.03	12	20.0	46.18	0.040	0.294	0.030	—	0.880	0.362	—
30	2.03	16	20.0	63.04	0.106	0.475	0.084	—	0.892	0.406	—
70	7.23	8	20.0	21.82	-0.043	-0.052	-0.075	—	0.371	0.154	—
70	7.22	12	20.0	36.72	-0.043	0.322	-0.078	—	0.437	0.169	—
70	7.35	16	20.0	48.26	-0.001	0.342	-0.037	—	0.477	0.201	—
70	7.36	24	20.0	71.88	0.016	0.176	-0.014	—	0.473	0.191	—
70	2.01	8	20.0	11.80	-0.151	-0.179	-0.219	—	0.657	0.171	—
70	2.01	12	20.0	21.88	-0.118	0.230	-0.195	—	0.774	0.235	—
70	2.01	16	20.0	32.98	-0.080	0.003	-0.153	—	0.813	0.276	—
70	2.01	24	20.0	54.17	0.007	0.356	-0.062	—	0.831	0.341	—
150	6.97	12	20.0	13.54	0.041	0.160	-0.007	—	0.339	0.141	—
150	7.11	18	20.0	23.60	0.115	0.259	0.074	—	0.456	0.254	—
150	7.13	24	20.0	29.90	0.074	0.379	0.006	—	0.447	0.214	—
150	7.12	32	20.0	40.98	0.096	0.177	0.060	—	0.476	0.253	—
150	2.02	12	20.0	9.70	-0.309	-1.378	-0.417	—	0.310	-0.099	—
150	2.05	18	20.0	15.26	-0.331	-0.355	-0.461	—	0.442	-0.051	—
150	2.05	24	20.0	21.88	-0.125	-0.357	-0.237	—	0.599	0.152	—
150	2.06	32	20.0	31.25	-0.142	-0.209	-0.267	—	0.637	0.149	—
250	6.96	24	20.0	10.73	-0.075	-0.353	-0.167	—	0.305	0.074	—
250	6.99	32	20.0	15.97	-0.125	-0.292	-0.230	—	0.319	0.048	—
250	6.99	36	20.0	18.36	-0.256	-0.783	-0.413	—	0.266	-0.059	—
250	2.03	24	20.0	11.80	0.047	0.240	-0.021	—	0.463	0.222	—
250	2.09	32	20.0	16.28	-0.116	-0.078	-0.232	—	0.468	0.124	—
250	2.11	36	20.0	18.36	-0.130	0.053	-0.256	—	0.501	0.129	—
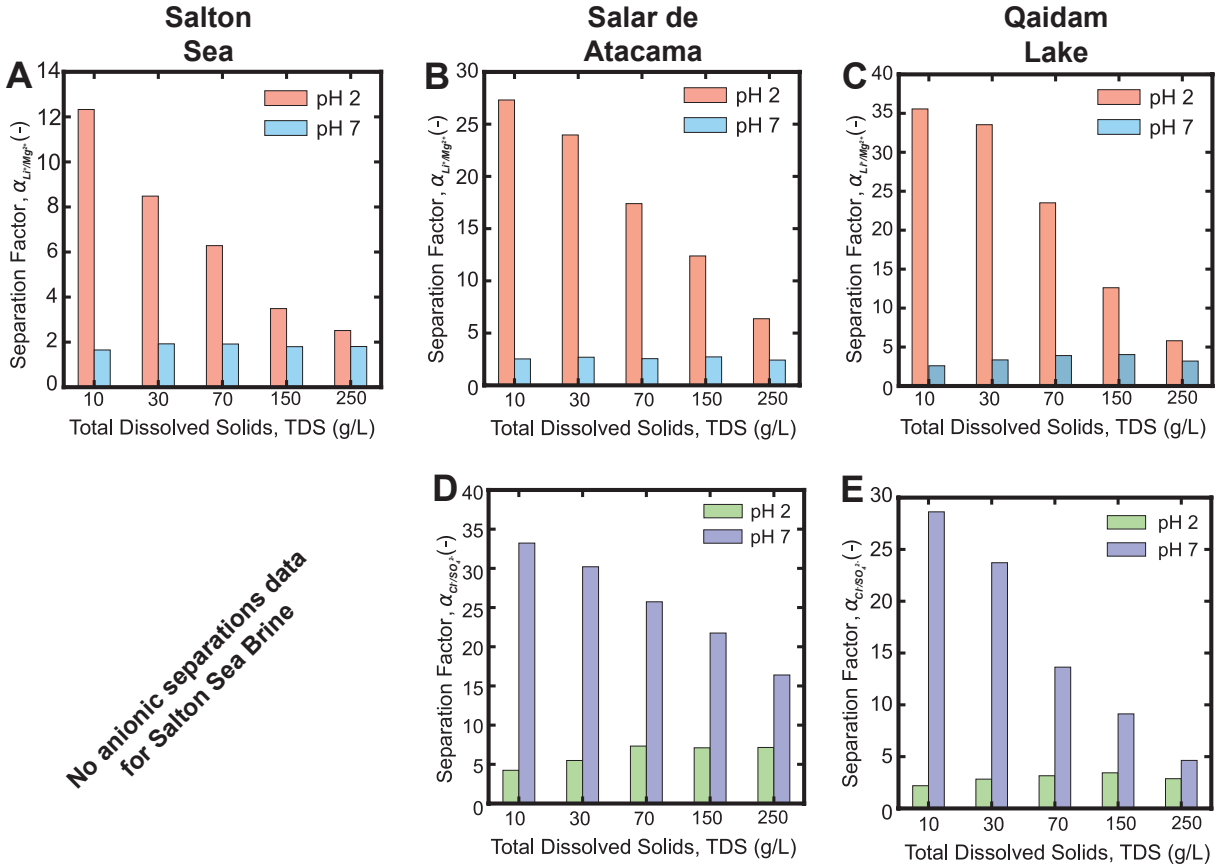
Supplementary Figure 2: Selectivity performance of NF 270 for Li-Mg separation, as a function of the solution pH and total dissolved solids (TDS) concentration, for inorganic brines from **A**) Salton Sea, United States, **B**) Salar de Atacama, Chile and **C**) Qaidam Lake, China. Selectivity performance of NF 270 for Cl^--SO_4^{2-} separation, as a function of the solution pH and total dissolved solids (TDS) concentration, for inorganic brines from **D**) Salar de Atacama, Chile and **E**) Qaidam Lake, China. For the cations, across all tested compositions, the separation factor remains largely invariant to TDS changes at pH 7, while exhibiting a decreasing trend with increasing TDS at pH 2. Vice versa, for the anions, the separation factor remains largely invariant to TDS changes at pH 2, while exhibiting a decreasing trend with increasing TDS at pH 7. This trend illustrates the significance of leveraging the Donnan exclusion mechanism, by using membranes with the same charge, to selectively separate ions with the same charges.

A.3 Simplified Synthetic Brine

To ascertain the impact of cation-anion coupling on the transport and monovalent selectivity of NF membranes, experiments with dual cation brine solutions are conducted. The composition of the dual cation solutions are depicted in Supp.Table 8. The molar ratios of Li^+ to Mg^{2+} of these dual cation solutions are kept constant at 1.75, in accordance to the Li^+-Mg^{2+} ratio of the Chilean brine.[3] To ensure valid comparisons with the multicomponent brine at 10 g/L TDS (0.35 M), the dual cation solutions are prepared at the same ionic molarity.

Supplementary Table 8: Nominal ionic composition of dual cation feed solutions based on brine from Salar de Atacama, at a solution molarity of 0.35 M.

Brine Composition (Abbreviation)	Nominal Composition (g/L)					Solution Molarity (M)
	Li^+	Mg^{2+}	Cl^-	SO_4^{2-}	TDS	
Li^+-Mg^{2+}-Cl^- (LM-C)	0.34	2.05	7.70	—	10.09	0.35
Li^+-Mg^{2+}-SO_4^{2-} (LM-S)	0.49	2.98	—	15.13	18.59	0.35
Li^+-Mg^{2+}-Cl^--SO_4^{2-} (LM-CS)	0.34	2.09	7.39	0.62	10.44	0.35

Three unique compositions are selected to elucidate the effects of anionic coupling on Li^+-Mg^{2+} selectivity. The three mixtures consist of: 1) lithium, magnesium and chloride ions (LM-C), 2) lithium, magnesium and sulfate ions (LM-S) and, 3) lithium, magnesium, chloride and sulfate ions (LM-CS). The molar ratio of chloride to sulfate ions in the LM-CS mixture is identical to that in the multicomponent Chilean brine. A summary of the experimental conditions and the measured species rejections is provided in Supp.Table 9. The feed pressures are selected so that the transmembrane water fluxes are close to that of the experiments with multicomponent solutions.

Supplementary Table 9: Experimental measurements for NF 270 based on dual cation brine at 0.35 M, at solution pH of 7 and 2.

Nominal Feed Molality (g/L)	Feed pH (-)	Feed Pressure (bar)	Temperature (°C)	Water Flux (LMH)	Species Rejection (-)			
					Li^+	Mg^{2+}	Cl^-	SO_4^{2-}
dual cation Brine (LM-C)								
0.35	6.94	6	20.0	28.98	−0.207	0.521	0.361	—
0.35	6.71	8	20.0	42.18	−0.184	0.600	0.427	—
0.35	6.83	10	20.0	54.17	−0.142	0.599	0.440	—
0.35	6.92	12	20.0	67.18	−0.125	0.653	0.467	—
0.35	2.09	6	20.0	15.10	−0.227	0.905	0.597	—
0.35	2.13	8	20.0	25.42	−0.125	0.970	0.660	—
0.35	2.13	10	20.0	39.55	0.029	0.949	0.686	—
0.35	2.14	12	20.0	53.64	0.115	0.975	0.717	—
dual cation Brine (LM-S)								
0.35	6.91	6	20.0	18.75	0.793	0.923	—	0.906
0.35	6.98	8	20.0	36.97	0.863	0.987	—	0.978
0.35	7.02	10	20.0	54.49	0.816	0.911	—	0.887
0.35	7.03	12	20.0	65.10	0.885	0.990	—	0.980
0.35	2.07	6	20.0	12.50	0.190	0.908	—	0.673
0.35	2.08	8	20.0	33.73	0.447	0.986	—	0.785
0.35	2.08	10	20.0	64.06	0.585	0.961	—	0.794
0.35	2.07	12	20.0	79.68	0.632	0.992	—	0.830
dual cation Brine (LM-CS)								
0.35	6.86	6	20.0	28.54	0.046	0.533	0.320	0.897
0.35	7.06	8	20.0	41.14	0.077	0.624	0.415	0.970
0.35	6.78	10	20.0	54.68	0.094	0.621	0.424	0.900
0.35	6.96	12	20.0	65.10	0.106	0.673	0.450	0.969
0.35	1.95	6	20.0	14.53	0.002	0.823	0.508	0.815
0.35	1.97	8	20.0	27.08	0.124	0.964	0.619	0.908
0.35	1.97	10	20.0	41.00	0.274	0.973	0.619	0.865
0.35	1.97	12	20.0	55.20	0.341	0.979	0.688	0.942

B   Computational Methods

B.1   Model Description

A pore flow model is used to analyze the selectivity of the membrane, and quantify the relative contributions arising from the partitioning and transport mechanisms. Here, we implement the Donnan-steric pore model with dielectric exclusion (DSPM-DE).[7–9] Starting from irreversible thermodynamics, the solute flux is linearized and proportional to the chemical potential gradient normal to the membrane surface. From this premise, the extended Nernst-Planck equation (Eq. 2) can be derived, which accounts for transport arising from concentration gradients, bulk solvent motion, and potential gradients.

$$J_i = K_{i,a}c_i J_w - K_{i,d}D_{i,\infty}\nabla c_i - K_{i,d}D_{i,\infty}\frac{z_i c_i F}{RT}\nabla\Psi \tag{2}$$

where J_i and J_w denote the solute and solvent fluxes, $K_{i,a}$ and $K_{i,d}$ denote the hindrance coefficients from advection and diffusion, c_i and z_i denote the molar concentration and electronic valency, $D_{i,\infty}$ denotes the Fickian diffusion coefficient, F and R denote the Faraday and ideal gas constants, and T and Ψ denote the temperature and electric potential.

The porous structure of the membrane is homogenized as rigid, tortuous cylinders with a constant surface diameter. Hindered transport theory[9] is applied to estimate the hindrance factors for both diffusion and advection, as provided in Eq. 3 and 4.

$$K_{i,d} = \frac{1 + \frac{9}{8}\lambda_i\ln\left(\lambda_i\right) - 1.56\lambda_i + 0.53\lambda_i^2 + 1.95\lambda_i^3 - 2.82\lambda_i^4 + 0.27\lambda_i^5 + 1.10\lambda_i^6 - 0.44\lambda_i^7}{\left(1 - \lambda_i\right)^2}, \text{for } \lambda_i \in [0, 0.95] \tag{3a}$$

$$K_{i,d} = 0.984\left(\frac{1 - \lambda_i}{\lambda_i}\right)^{5/2}, \text{for } \lambda_i \in (0.95, 1] \tag{3b}$$

$$K_{i,a} = \frac{1 + 3.867\lambda_i - 1.907\lambda_i^2 - 0.834\lambda_i^3}{1 + 1.867\lambda_i - 0.741\lambda_i^2} \tag{4}$$

S17

where λ_i denotes the ratio of the solute's Stokes radius to the pore radius of the membrane.

For chemical stability, electroneutrality conditions are imposed on the solutions within and external to the membrane pores, as shown in Eq. 5 and 6.

$$\sum_i^N z_i c_i = 0 \tag{5}$$

$$\chi_d + \sum_i^N z_i c_i = 0 \tag{6}$$

where χ_d represents the charge density of the membrane active layer.

Under this approach, the solute fluxes between two unique *uncharged* species are not explicitly coupled[10] (e.g. the concentration gradient of one species does not influence the transport rate of another species); The transport between unique *charged* species, however, are implicitly coupled through the induced potential gradient across the active layer, to maintain electroneutrality of the solutions.

Isoactivity conditions, as described by Eq. 7, are applied along the solution-membrane interface, ensuring that the species Gibbs free energy remains continuous.[11] Here, the solute's effective partition coefficient is defined as the ratio of the solute activity in the membrane pore relative to the bulk solution. Solute partitioning is modeled as the combination of three factors: 1) steric exclusion arising from size-based filtration by the membrane pores, 2) Donnan exclusion arising from charge screening of ions due to the Donnan potential across the solution-membrane interface, and 3) dielectric exclusion arising from a solvation energy barrier for the ions.

$$\frac{(\gamma_i c_i)_{mem}}{(\gamma_i c_i)_{bulk}} = \Phi_{i,steric} \; \Phi_{i,Donnan} \; \Phi_{i,dielectric} \tag{7}$$

where γ_i denotes the activity coefficient of solute i, and Φ_i denotes the partition coefficient.

Steric exclusion arises due to the size difference between dissolved solute and the membrane pore. Solutes that are larger than the membrane pore radius are incapable of transmembrane passage. Unlike point charges, solutes that are smaller than the membrane pore,

however, exhibit a size-dependent passage probability that can be approximated by a geometric distribution, as provided in Eq. 8.[8]

$$\Phi_{i,steric} = (1 - \lambda_i)^2, \text{ for } \lambda_i \in [0, 1] \tag{8a}$$

$$\Phi_{i,steric} = 0, \quad \text{otherwise} \tag{8b}$$

Across the solution-membrane interface, a potential difference (Donnan potential) exists due to differences in the ion concentrations between the two media. The partition coefficient due to the Donnan potential is governed by Eq. 9, which is analogous to the Nernst equation. As a result, ions that are opposite in charge to the Donnan potential will selectively partition into the pores, while ions that are similar in charge to the Donnan potential will be selectively excluded from partioning.[12]

$$\Phi_{i,Donnan} = \exp\left(-\frac{z_i F}{RT}\,\Delta\Psi_D\right) \tag{9}$$

where $\Delta\Psi_D$ denotes the Donnan potential of the active layer.

In addition to size sieving and charge screening effects, the relative permittivity of the solvent (dielectric constant) can be considerably lowered within the membrane pores. This is a result of the constrained mobility and orientation of free and hydrating waters arising from nanoscale confinement. In nanoscale channels, dielectric exclusion arises from the weakening of water-ion interactions within the membrane pores, posing an energy barrier that may induce ion dehydration during ion partitioning;[12–14] however, the precise mechanistic relationship between dielectric exclusion and ion dehydration remains an active area of research and is beyond the scope of our present work. This energy barrier can be estimated based on solvation energies or image forces.[9] As a first approximation to the former, the Born model is commonly adopted,[15] as given in Eq. 10.

$$\Phi_{i,dielectric} = \exp\left[-\frac{z_i^2 e^2}{8\pi k_B T \epsilon_0 r_i}\left(\frac{1}{\epsilon_{mem}} - \frac{1}{\epsilon_{bulk}}\right)\right] \tag{10}$$

where ϵ_{mem} and ϵ_{bulk} denote the relative permittivity in the membrane pore and bulk solution.

During membrane filtration, concentration boundary layers form along the membrane–solution interface, arising from the selectivity of the polyamide active layer.[16] Here, concentration polarization effects are incorporated to accurately model the ion concentrations along the membrane–solution interface, using the model proposed by Geraldes and Alves.[7] Within the concentration boundary layers, the total ion flux is contributed from diffusive, convective and electromigrative fluxes, as given in Eq. 11.

$$J_i = \bar{k}_{i,c}\left(c_{i,int} - c_{i,b}\right) + J_w c_{i,int} - z_i c_{i,int} D_{i,\infty}\zeta_{int}\frac{F}{RT} \tag{11}$$

where $c_{i,int}$ and $c_{i,b}$ denote the ion concentration along the membrane–solution interface, and in bulk solution, ζ_{int} denotes the electric potential gradient along the membrane–solution interface and $\bar{k}_{i,c}$ represents the modified mass transfer coefficient accounting for the 'suction effect'.[17] The modified mass transfer coefficient can be calculated from conventional mass transfer coefficients, as provided in Eq. 12.

$$\bar{k}_{i,c} = k_{i,c}\left[\Xi + \left(1 + 0.26\,\Xi^{1.4}\right)^{-1.7}\right] \tag{12}$$

where $\Xi = J_w/k_{i,c}$.

The mass transfer coefficient is computed from the mass transfer correlation from a prior study for our bench-scale apparatus, incorporating mixing effects from the spacer.[18]

$$k_{i,c} = 1.121 * 10^{-4} * \left(\frac{v_w}{0.239}\right)^{0.79} \tag{13}$$

where v_w denotes the cross-flow velocity.

Overall, the key modeling assumptions can be summarized as:

1. Solute transport across the membrane is one-dimensional, normal to the area of the active layer.

2. Electroneutrality is maintained in the membrane pores and the bulk solution under steady-state conditions.

3. The ions are fully dissociated in water, and the dissolved solutes are modeled as hard spheres, consisting of a charged ion surrounded by a sphere of hydrating water molecules.

4. Membrane charge density and pore radius are modeled homogeneously, based on the statistical average value. Membrane pores are modeled as tortuous cylinders.

5. Hindrance factor formulations based on the transport of hard spheres in neutral cylindrical pores are applicable to the transport of charged species across charged porous membranes.

6. Solute transport between uncharged species are fully decoupled, while the transport between charged species are only coupled through the electric potential.

B.2   Numerical Methods

The DSPM-DE model is developed in Python, using the NumPy and SciPy property packages. The governing differential equations for transport (Eq. 2) are discretized with a second-order centered difference method, using a structured mesh with 100 nodes. The boundary conditions for solute concentrations and electric potential are imposed by the isoactivity conditions (Eq. 7). Electroneutrality conditions, as provided by Eq. 5 and 6, are used to close the system of equations. The nodal species concentrations and electric potential are solved simultaneously, using the method of successive over-relaxation with a relaxation factor of 1.6, with a convergence tolerance of 10^{-8}.

²⁷⁰ The dual annealing algorithm, which is a metaheuristic stochastic optimization algorithm, is used to fit the membrane parameters of DSPM-DE. Unlike direct gradient based methods, the dual annealing algorithm prescribes non-zero probability for the acceptance of sub-optimal solutions during numerical iteration. This ensures that the algorithm does not converge into local optimums. To ensure reproducibility and high accuracy of the numerical solution, a local search algorithm based on the Nelder-Mead method is implemented at each step of the stochastic algorithm. The convergence tolerance for the optimization problem is set at 10^{-4}.

B.3 Experimental Comparisons

Here, we compare the numerical predictions from the DSPM-DE model to experimental data found in the literature. Using original model parameters from Micari et al.[1] and Labban et al.,[2] respectively, the model results are juxtaposed against the experimental measurements in Supp. Fig. 3A and B. The maximum absolute deviation is less than 15 % and 8 % for the data from Micari et al. and Labban et al., respectively. The model is able to capture transport coupling between ions, as evident by its ability to reproduce the negative rejection phenomena of small monovalent ions (e.g. Na^+ and Cl^-).[16]
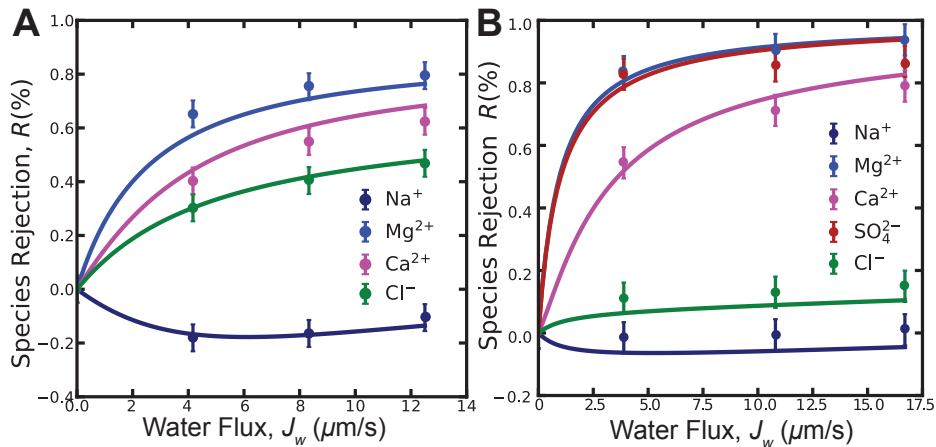
Supplementary Figure 3: Model validation for the Donnan-steric pore model with dielectric exclusion, using original experimental measurements and model parameters from **A**) Micari et al.,[1] and **B**) Labban et al.,[2] respectively.
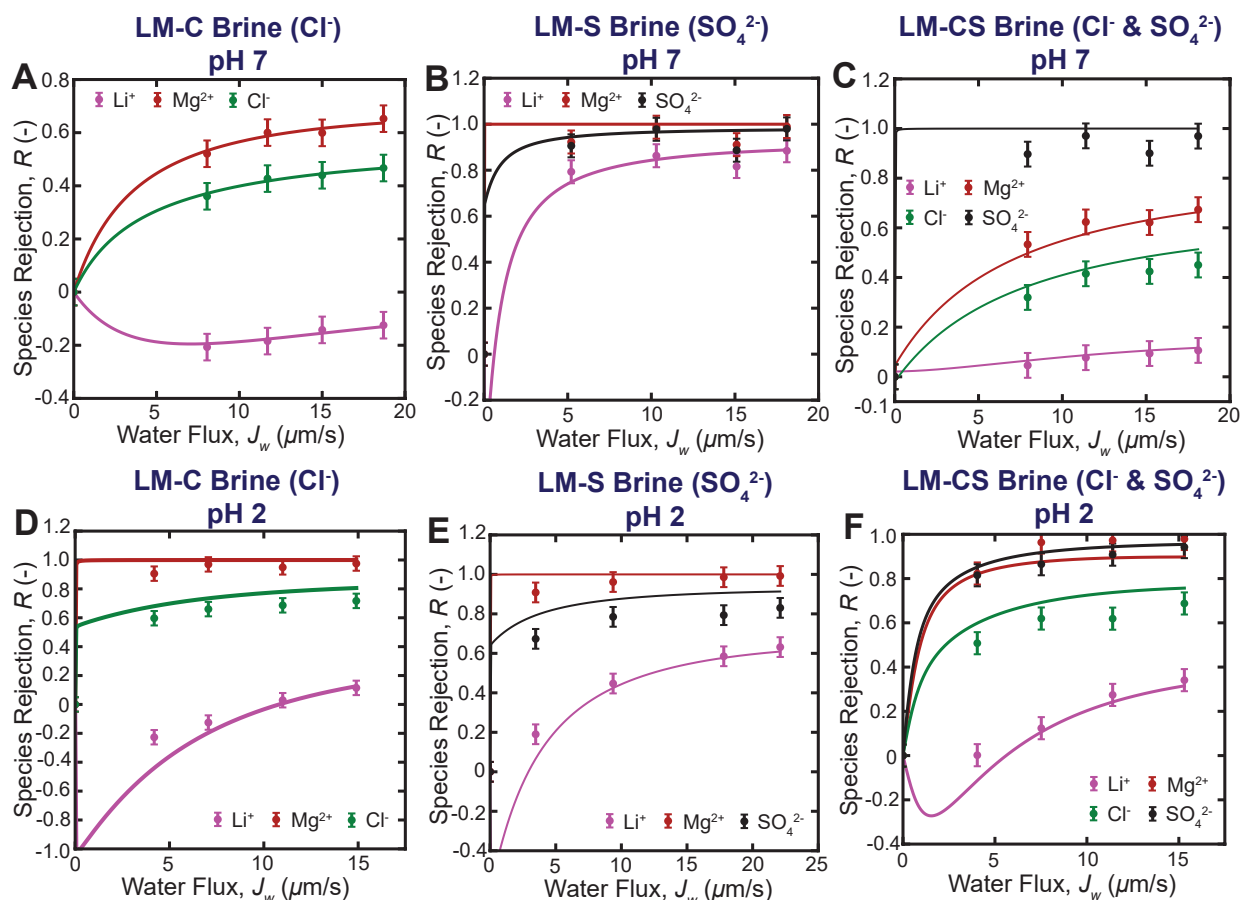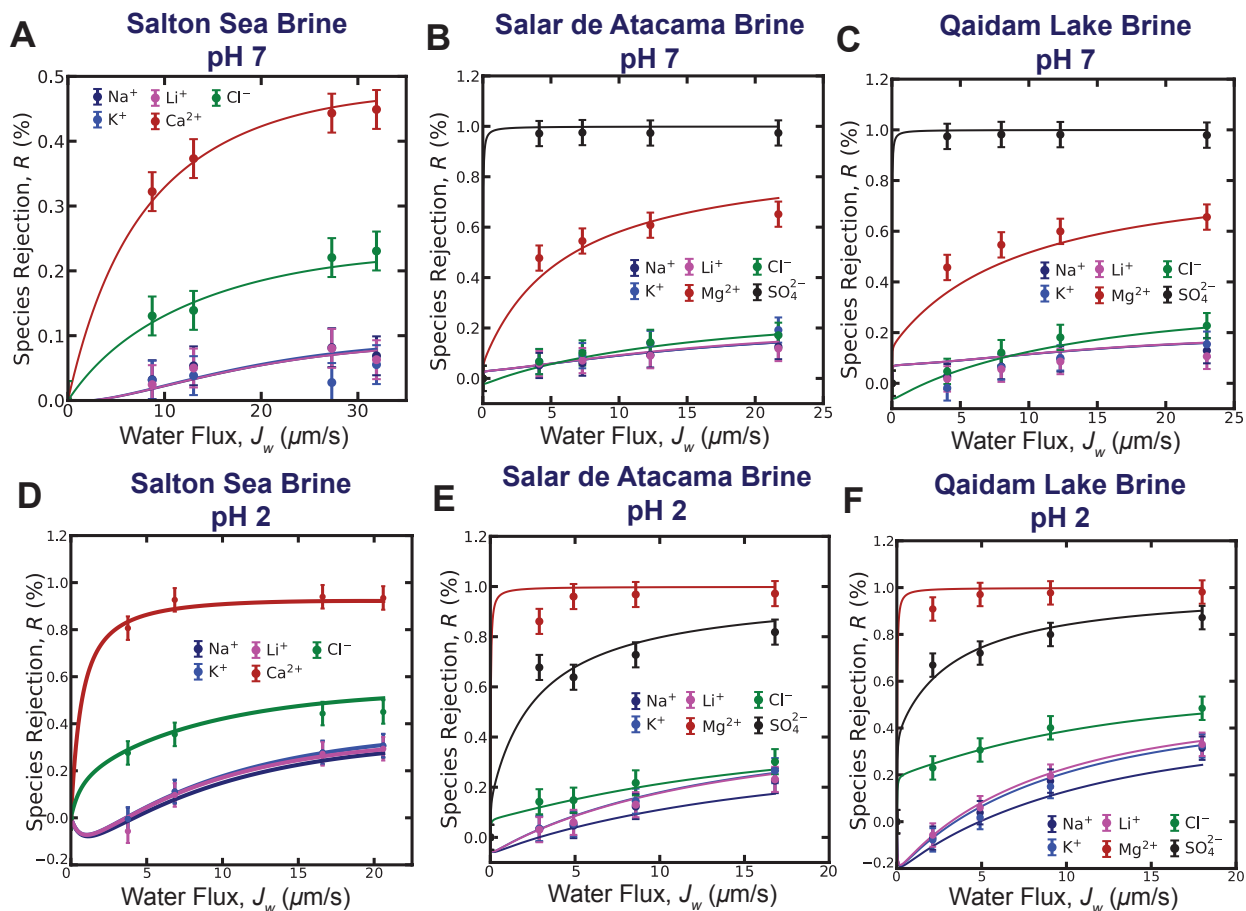
Supplementary Figure 4: Plots of the species rejection against the transmembrane water flux from the nanofiltration experiments with **A**) simulated LM-C brine at pH 7; **B**) simulated LM-S brine at pH 7; **C**) simulated LM-CS brine at pH 7; **D**) simulated LM-C brine at pH 2; **E**) simulated LM-S brine at pH 2; **F**) simulated LM-CS brine at pH 2; Solid curves denote model predictions while solid markers denote experimental measurements.

For the original experiments presented in Supp.Table 5, 6, 7 and 9, the model parameters from DSPM-DE are fit using the algorithms described earlier. In total, 4 model parameters are obtained from a total of 72 ion rejection measurements, for each solution pH. The results are summarized in Supp.Table 10.

Supplementary Table 10: Regressed model parameters for DSPM-DE from the respective experimental data.

Solution pH	Effective Thickness ΔX (nm)	Average Pore Radius r_p (nm)	Relative Permittivity ϵ (-)	Volumetric Charge Density χ (mol/m^3)
7	60.06	0.416	39.58	-63.57
2	185.38	0.461	34.00	6.91

The agreement between the model and experimental measurements for nanofiltration

Supplementary Figure 5: Plots of the species rejection against the transmembrane water flux from the nanofiltration experiments with **A**) Salton sea brine at pH 7; **B**) Salar de Atacama brine at pH 7; **C**) Qaidam lake brine at pH 7; **D**) Salton sea brine at pH 2; **E**) Salar de Atacama brine at pH 2; **F**) Qaidam lake brine at pH 2; Solid curves denote model predictions while solid markers denote experimental measurements.

Supplementary Table 11: Comparison between the limiting rejection of neutral solute between DPSM-DE and prior experimental measurements.[2]

Neutral Solute	Molecular Weight (Da)	Stokes Radius (nm)	Model Limiting Rejection (-)	Experimental Solute Rejection (-)
Glucose	180.0	0.36	0.489	0.535
Sucrose	342.0	0.46	0.739	0.802
Raffinose	504.0	0.54	0.841	0.879

with the dual cation brine solutions are presented in Supp. Fig. 4A - F. The root-mean-square residual between the model and experiments is 2.2 %.

Similarly, the experimental measurements and model predictions for nanofiltration with

the multicomponent salt-lake brines at 10 g/L concentration are illustrated in Supp. Fig. 5A - F. The root-mean-square residual between the model and experiments is 2.8 %. Using the regressed model parameters, the predictions of the limiting rejection for three neutral solutes are summarized in Supp. Table 11, leveraging empirical measurements from an earlier publication from our group.[2] The maximum deviation between the model estimates and the experimental measurements is 8.5 %.

C Results & Analysis

C.1 Solute Partitioning

In this section, we quantify the relative contributions of steric, dielectric and Donnan exclusions to the performance of NF 270 for Li^+ - Mg^{2+} separation. Multicomponent salt-lake brines, at a concentration of 10 g/L, are used to elucidate the partition coefficients of the three mechanisms. To ensure valid comparisons between the different brines and solution pH levels, the transmembrane water flux is fixed at 15 μm/s. The validated DSPM-DE model presented in Supp. Fig. 4 and 5 is used to interpolate between the experimental points for this comparison.

The schematic diagrams of the thermodynamic partition coefficients for steric, dielectric and Donnan exclusions are presented in Supp. Fig. 7A - F. Partition coefficients that are less than 1 indicate that the activity of the solute is lower in the membrane pore as compared to the bulk solution, and vice versa. The effective partition coefficient of a solute is the product of the three constituent partition coefficients, which is summarized in Supp.Table 12.

Supplementary Table 12: Ion effective partition coefficients with multicomponent & dual cation brine for NF 270 at transmembrane water fluxes of 15 μm/s.

Brine	pH	Effective Partition Coefficients						
		Na^+	K^+	Li^+	Mg^{2+}	Ca^{2+}	Cl^-	SO_4^{2-}
Salton Sea	7	0.4877	0.3080	0.4413	—	0.0747	0.0023	—
Salton Sea	2	0.0221	0.0103	0.0287	—	0.0002	0.1054	—
Qaidam Lake	7	0.4891	0.3088	0.4425	0.0493	—	0.0023	<0.0001
Qaidam Lake	2	0.0117	0.0049	0.0155	<0.0001	—-	0.0647	0.0027
Salar de Atacama	7	0.3378	0.2671	0.3134	0.0651	—	0.0039	0.0012
Salar de Atacama	2	0.0092	0.0036	0.0125	0.0001	—-	0.0490	0.0015
Dual Cation (LM-C)	7	—	—	0.5744	0.1760	—	0.0245	—
Dual Cation (LM-C)	2	—	—	0.0260	0.0003	—	0.1924	—
Dual Cation (LM-S)	7	—	—	0.0007	<0.0001	—	—	0.0056
Dual Cation (LM-S)	2	—	—	0.0015	<0.0001	—	—	0.0026
Dual Cation (LM-CS)	7	—	—	0.3658	0.0557	—	0.0407	0.0011
Dual Cation (LM-CS)	2	—	—	0.0159	0.0005	—	0.0647	0.0017

Across the 6 panels, the effective partition coefficients of the dissolved solutes are less than 1, indicating that the active layer is ion rejecting. This deduction is consistent with our prior understanding of semi-aromatic thin film polyamides.[19] Furthermore, between the 7 different ions, the magnitude of steric exclusion increases with the Stokes radius for all the solutes, a result that aligns with hindered transport theory.[20] The partition coefficient for dielectric exclusion is lower for smaller ions with higher electronic valency. This observation parallels our expectations from solvation theory,[15,21,22] where ions with higher charge densities (Mg^{2+}, Ca^{2+} & SO_4^{2-}) experience a larger solvation energy barrier in response to the decreasing relative permittivity of water.

The isoelectric point (IEP) of a membrane is defined as the pH level at which the active layer exhibits a net neutral charge density. This phenomenon arises from the interactions between the solution and, the carboxyl and amino functional groups along the polyamide chains.[23] At the IEP, charged solutes experience little-to-no Donnan exclusion effects. From prior work, the IEP of NF 270 was determined to be between the pH of $3-5$.[1,2,20] As depicted in Supp. Fig. 6, using zeta potential measurements, the IEP was estimated to between the pH of 2.95 and 3.20. Here, solution pH levels are selected to be above and below the IEP, to analyze the effects of Donnan exclusion on the ion rejection characteristics of NF 270.

At a solution pH of 7, we observe that the Donnan exclusion partition coefficients of the cations are consistently greater than unity, indicative of its selective permeance into the active layer. Concurrently, the anions are excluded because the partition coefficients remain smaller than unity. This Gibbs-Donnan effect is consistent with our findings. Based on the characterization of the membrane, DSPM-DE suggests that the active layer exhibits a negative charge density at pH 7, as described in Supp.Table 10. As a result, the Donnan potential enhances the rejection of anions. For cations, however, the same Donnan potential enhances its permeation into the active layer, leading to a reduction in cationic rejection. This mechanism aligns with our experimental measurements, as presented in Supp. Fig. 5.

At a solution pH of 2, however, the membrane exhibits a net positive charge density,

³⁴² as described in Supp.Table 10. The predictions based on Donnan equilibrium theory are

³⁴³ also exemplified in our experimental measurements, as depicted in Supp. Fig. 4 and 5.

³⁴⁴ Likewise, the opposite effect from the Gibbs-Donnan effect is observed. Consequently, under

³⁴⁵ the influence from a positive Donnan potential, the cations are selectively excluded, but vice

³⁴⁶ versa for the anions.

³⁴⁷ Furthermore, we observe that the intensity of the Gibbs-Donnan effect is stronger for

³⁴⁸ multivalent ions, leading to extremely high rejections of Mg^{2+} at pH 2. This phenomenon

³⁴⁹ accounts for the observed differences between the cationic and anionic selectivities in Supp.

³⁵⁰ Fig. 2. Consequently, at pH 7, the separation factor for Li^+ - Mg^{2+} is considerably lower,

³⁵¹ while the corresponding separation factor for Cl^- - SO_4^{2-} is magnified, across all the tested

³⁵² brines. The opposite effect is observed at pH 2, explaining the high measured Li^+ - Mg^{2+}

³⁵³ separation factors at all tested salinities. The results underscore the importance of optimizing

³⁵⁴ the Donnan potential of the active layer to optimize charge-based separation of ions.
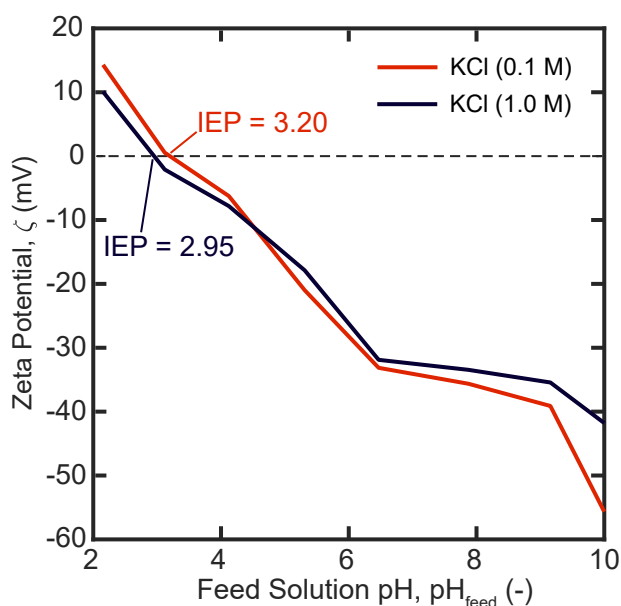
Supplementary Figure 6: Plot of the zeta potential as a function of the feed solution pH. The isoelectric point was determined to be between the solution pH of 2.95 - 3.20, using 0.1 – 1.0 M KCl solutions.
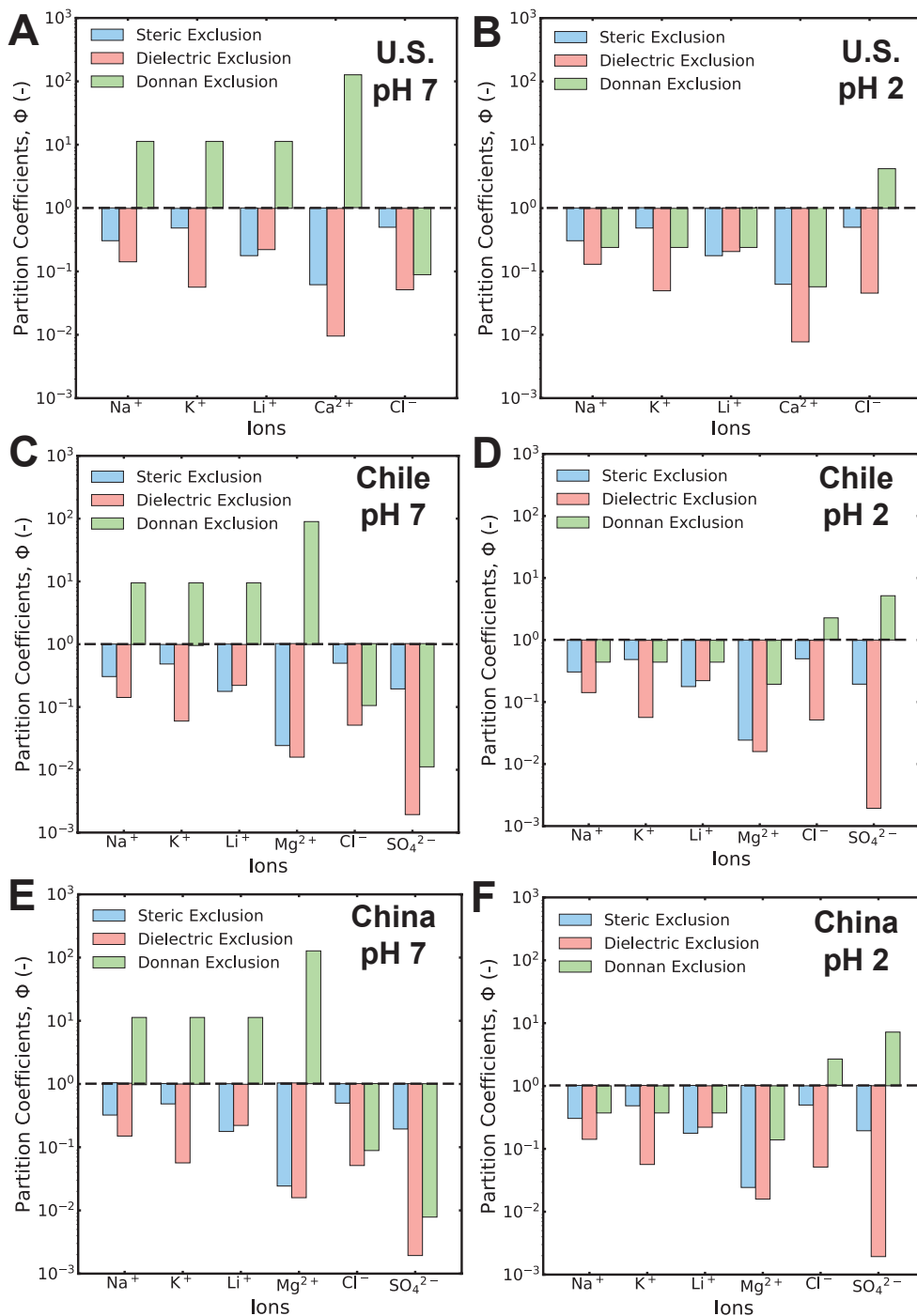
Supplementary Figure 7: Schematic diagrams of the thermodynamic partition coefficients for the ionic species at a total dissolved solids concentration of 10 g/L. The relative contributions from steric, dielectric and Donnan exclusions, are outlined in blue, red and green, respectively. The sub-panels correspond to: **A**) Salton sea brine at pH 7; **B**) Salton sea, United States brine at pH 2; **C**) Salar de Atacama, Chile brine at pH 7; **C**) Salar de Atacama, Chile brine at pH 2; **E**) Qaidam Lake, China brine at pH 7; **F**) Qaidam Lake, China brine at pH 2.

C.2 Transport Mechanics

In this section, we leverage our calibrated computational model to infer the key transport characteristics of nanofiltration with multicomponent solutions. Consistent with the *Solute Partitioning* section, the comparisons are conducted at a fixed transmembrane water flux of 15 μm/s, and a feed TDS concentration of 10 g/L. Our numerical findings are summarized in Supp. Fig. 8A - B and 9A - F.

Evidence of transmembrane transport coupling between ions is well documented in the literature, based on molecular dynamics (MD) simulations [14,24] and multi-ionic experiments. [2,10,25] Due to high computational complexities and costs, the molecular simulations are largely restricted to simple pore geometries with dual cation mixtures. For MD simulations involving Na^+ and Cl^- ions, Cl^- was reported to preferentially traverse across the membrane pore, owing to lower free energy barriers from favorable interactions with the pore interior. [14,26] The ensuing charge anisotropy results in a reverse electric potential across the pore, inducing an electrostatic pullback that impedes Cl^- forward transport. The same induced electric potential was reported to accelerate the forward transport of Na^+ to achieve solution electroneutrality.

In this work, the extended Nernst-Planck model is used to investigate the significance of such inter-ionic transport coupling in multicomponent brines. The normalized ionic fluxes of the three multicomponent brines, at pH 7, are presented in Supp. Fig.9A, C and E. Across the three tested compositions, our numerical results suggest that Cl^- and SO_4^{2-} transport is largely driven by diffusion, as illustrated in Supp. Fig. 8A. Macroscopically, this phenomenon is a result of the large diffusion and hindrance coefficients of Cl^-, as well as the large concentration gradient established by the poor solute partitioning. [16]
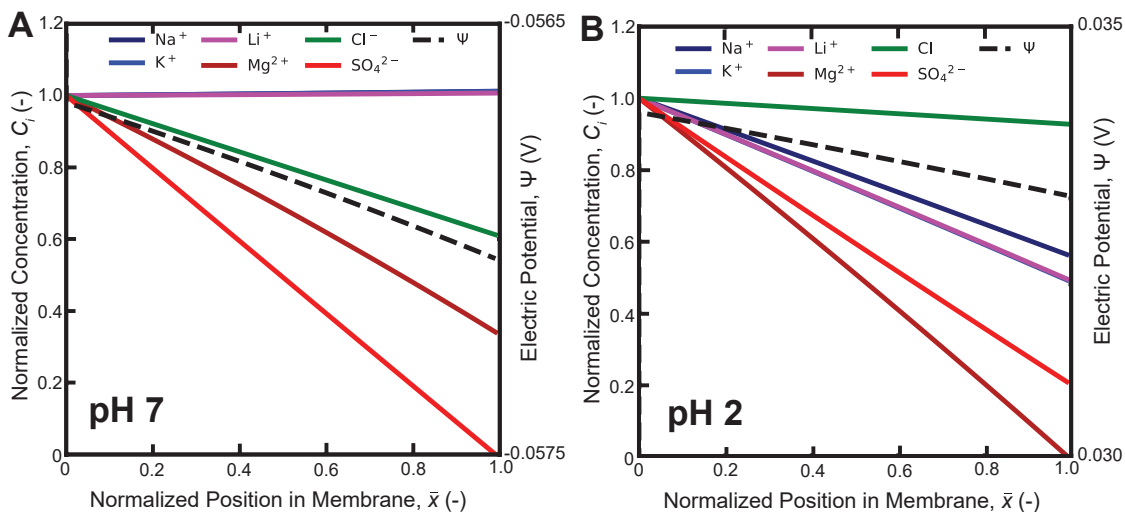
Supplementary Figure 8: Plots of the normalized species concentrations (solid curves) and local electric potential (dotted curves) within the active layer of the nanofiltration membrane at **A**) pH 7, and **B**) pH 2, respectively. The species concentrations are normalized to the feed-side of the active layer, following species partitioning with the solution.

From Supp. Fig. 8A & B, our model suggests that the ensuring charge anisotropy from the anionic permeation leads to an uneven electric potential across the membrane pore. The induced electric field accelerates the kinetics of cation permeation, a process known as electromigration. For the monovalent cations (Li^+, Na^+ & K^+), our model evinces that electromigration plays a critical role in its forward transport, as evident from Supp. Fig. 9A, C and E. To achieve solution electroneutrality under steady state conditions, the forward transport of the monovalent cations is counteracted by a reverse diffusive flux. These observations on the transport coupling between monovalent anions and cations appear to be consistent with the prior results from the molecular-scale modeling with dual cation salt solutions.[14,24,26]

On the contrary, the effect of electromigrative coupling is less prevalent for the multivalent cations. Due to its poor partitioning into the membrane, our model suggests that the concentration of multivalent ions within the active layer is sparse. The multivalent ionic fluxes, as depicted in Supp. Fig. 9A, C and E, are at least one order of magnitude lower than the corresponding values for monovalent ions. From classical transport theory, in the limit

of infinite dilution, the species fluxes decouple and become independent from each other.[17,27] Due to its low concentrations, our model suggests that the ionic fluxes of Mg^{2+} and Ca^{2+} are relatively unaffected by the charge anisotropy, which appears to be consistent with the classical theories. Consequently, from our simulations, the mutivalent ionic fluxes appear to be diffusive in nature.

Supp. Fig 9B, D & E illustrate the normalized ionic fluxes under the influence of a positive surface charge density. From experimental measurements, we observe that the water permeability of the membrane decreased by approximately 40 %, when the pH is lowered from 7 to 2. Recent NF experiments involving pH changes attributed the reduction in water permeability to physical restructuring of the polyamide layer.[28] Based on the regressed parameters in Supp.Table 10, our model suggests likewise, that the permeability reduction is largely due to the lowering of the active layer porosity-tortuosity coefficient.

Across the three tested compositions, the absolute ionic fluxes of each species reduced by approximately 40 %. Assuming a 20 nm thick polyamide layer, our model suggests a reduction in porosity-tortuosity coefficient by 23 % when the pH is lowered to 2, causing the membrane to become denser. This ionic flux reduction arises from weakening advective and electromigrative coupling. Consequently, this combination causes the transport to converge to similar predictions from the solution-diffusion theory; the species transport becomes decoupled and diffusive in nature.
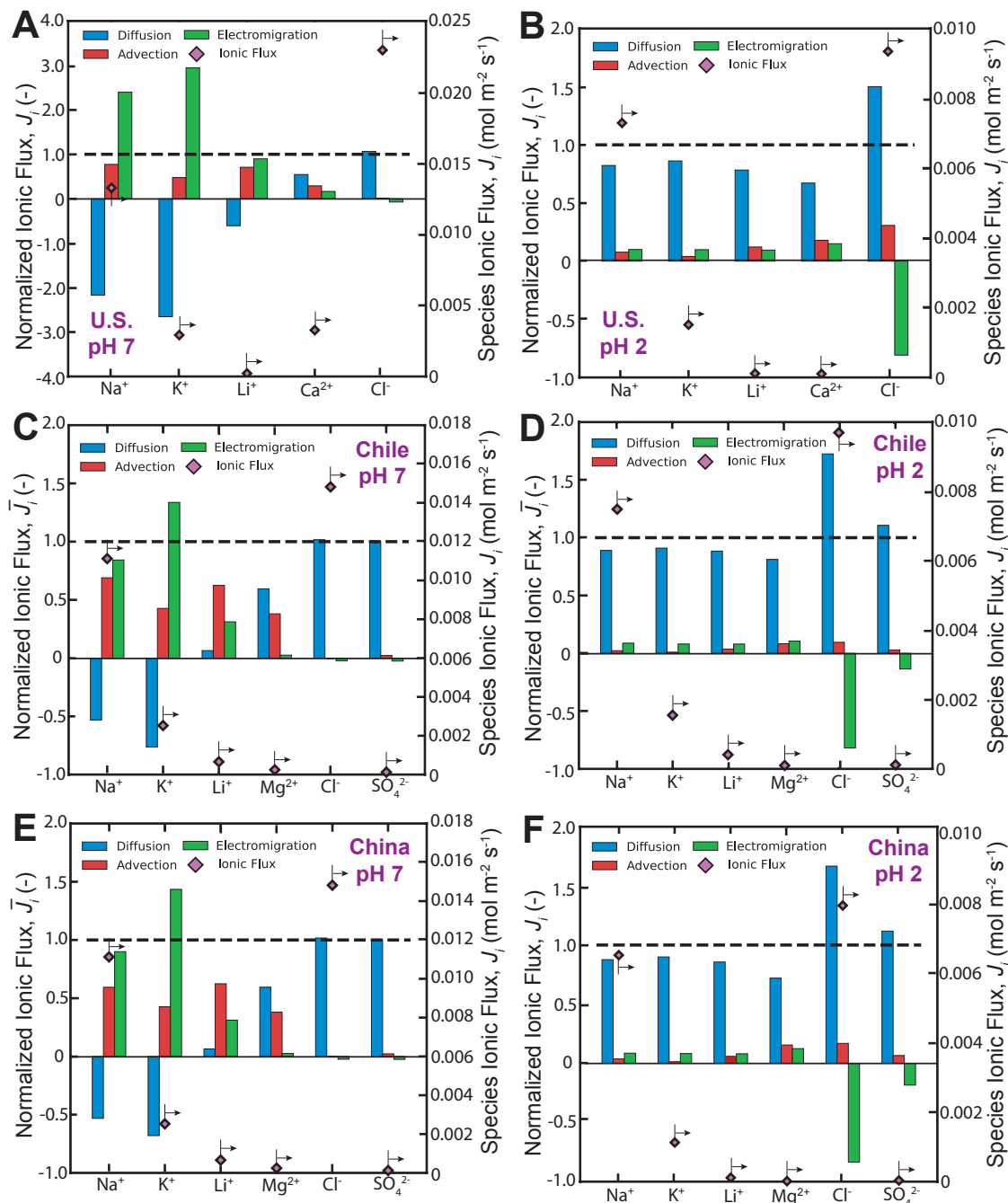
Supplementary Figure 9: Schematic diagrams of the transport mechanisms for the ionic species, at a total dissolved solids concentration of 10 g/L. The normalized diffusive, advective and electromigrative fluxes for the ionic species are represented in blue, red and green, respectively. The ionic fluxes of the three distinct mechanisms are normalized to the net species flux. The normalized fluxes, therefore, will sum to 1 (dotted lines). The sub-panels correspond to: **A**) Salton sea brine at pH 7; **B**) Salton sea, United States brine at pH 2; **C**) Salar de Atacama, Chile brine at pH 7; **C**) Salar de Atacama, Chile brine at pH 2; **E**) Qaidam Lake, China brine at pH 7; **F**) Qaidam Lake, China brine at pH 2.

C.3   Composition Simplifications

Here, we compare the differences in the rejection of Li^+ and Mg^{2+} ions, between the dual cation and actual multicomponent salt-lake brine. The errors for Li^+ and Mg^{2+} are plotted in up and down triangles, for solution pH of 7 and 2, in Supp. Fig. 10A & B, respectively. The dual cation experim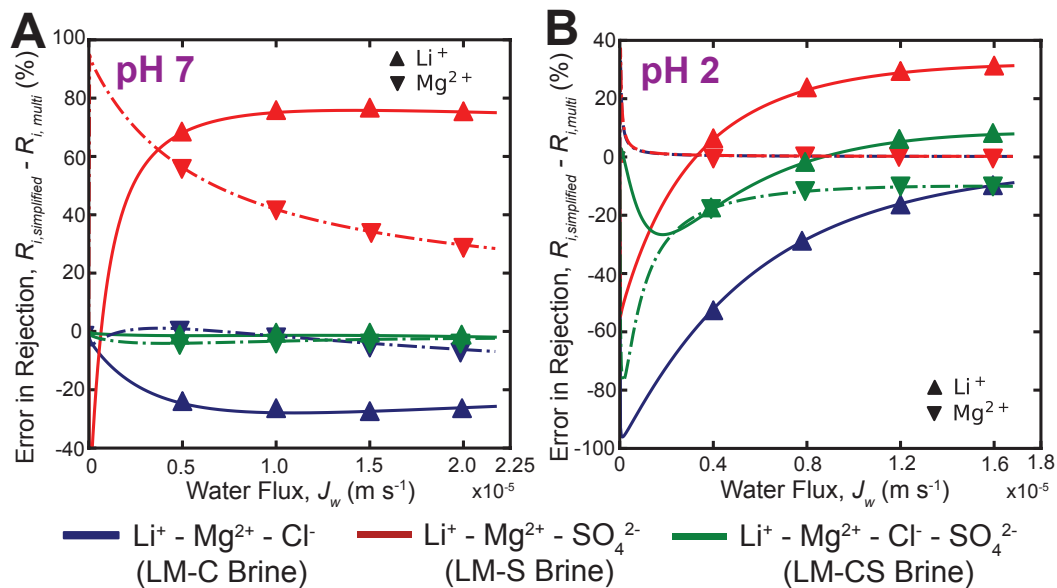ents used in this analysis are outlined in Supp.Table 8, and the multicomponent experiments correspond to the 10 g/L data presented in Supp.Table 1. The plots in Supp. Fig 10 are obtained by interpolating between the experimental measurements, using the validated model presented in the previous sections.

Supplementary Figure 10: Plot of the error in species rejection (defined as the difference between dual cation brines and multicomponent salt-lake brines at the same feed molarity) against the transmembrane water flux at **A**) pH 7; and **B**) pH 2, respectively. Simulated brine that mimics both the cation and anion ratios (green lines and markers) register maximum rejection error of 4 % and 15 % at pH 7 and 2, respectively, for both Li^+ & Mg^{2+}, while dual cation brines with only one anion, Cl^- (blue) or SO_4^{2-} (red), register rejection errors up to 80 % for both pH levels.

In the previous section, we documented evidence of transport coupling between cations and anions, due to electromigration from the induced potential gradient. In the literature, however, when new membranes are characterized, the anionic compositions of the feed solutions are often simplified. Here, we are interested to evaluate the effect of this simplification

424 on the separation factor of Li^+- Mg^{2+}.

425 Supp. Fig. 10A illustrate the species rejection error against the transmembrane water

426 flux, at a solution pH of 7. The LM-C, LM-S and LM-CS brine results are graphed in blue,

427 red and green, respectively. For solutions with one anion, the errors in species rejection are

428 large for the LM-C and LM-S brines, registering maximum absolute errors of 80 % for Li^+,

429 and 25 % for Mg^{2+}. When the anionic composition is accurately replicated with the LM-CS

430 brine, the corresponding absolute errors for Li^+ and Mg^{2+} fall under under 4 % for both

431 ions. Similar observations are registered under a solution pH of 2, as illustrated in Supp.

432 Fig. 10B.

433 The differences in cationic rejection can be attributed to transport coupling with the

434 anions, to preserve electroneutrality in the permeate solution. In the absence of SO_4^{2-} ions,

435 as represented by the LM-C feed brine, the anionic flux is significantly overestimated. This

436 arises from the high effective partition coefficient and diffusive flux of the Cl^- ions, as dis-

437 cussed in the previous sections. A stronger electric potential gradient than that with the

438 multicomponent brine is induced, increasing the transmembrane cationic flux. Given that

439 the effective partition coefficient of Li^+ is about one order of magnitude greater than that

440 of Mg^{2+}, Li^+ is preferentially transported over Mg^{2+}. The rejection of Li^+, consequently,

441 falls due to its higher permeance, while its effect on the rejection of Mg^{2+} is less significant;

442 this mechanism explains the observed differences in rejection with the LM-C brine in Supp.

443 Fig. 10A & B.

444 When Cl^- ions are absent in the feed solution, as mimicked by the LM-S brine, the op-

445 posite effect occurs. The transmembrane anionic flux falls by 80 % approximately, due to

446 the low effective partition coefficient of SO_4^{2-} ions. To preserve electroneutrality, the corre-

447 sponding cationic fluxes of Li^+ and Mg^{2+} decrease proportionally, magnifying its rejection.

448 This explains the elevated rejections of Li^+ and Mg^{2+} observed in Supp. Fig. 10A & B.

449 Lastly, when both Cl^- and SO_4^{2-} ions are represented in the feed solution, as illustrated

450 by the LM-CS brine, the rejection errors for the cations decrease to be under 4 % at pH

7, and under 15 % at pH 2. We speculate that the higher errors at pH 2 arose from competition from Na^+ and K^+ for partitioning, due to Donnan exclusion from the positively charged membrane. Based on the rejection values, the errors in the Li^+ - Mg^{2+} separation factor are consistently under 15 %, for both solution pH. These findings demonstrate a causal relationship between cation-anion transport coupling and the derived separation factors; future membrane characterizations should utilize solutions with the appropriate anionic compositions, to obtain accurate simulation of the transport phenomena of salt-lake brines.

References

(1) Micari, M.; Diamantidou, D.; Heijman, B.; Moser, M.; Haidari, A.; Spanjers, H.; Bertsch, V. Experimental and theoretical characterization of commercial nanofiltration membranes for the treatment of ion exchange spent regenerant. *Journal of Membrane Science* **2020**, *606*, 118117.

(2) Labban, O.; Liu, C.; Chong, T. H.; Lienhard, J. H. Relating transport modeling to nanofiltration membrane fabrication: Navigating the permeability-selectivity trade-off in desalination pretreatment. *Journal of Membrane Science* **2018**, *554*, 26–38.

(3) Park, S. H.; Kim, J. H.; Moon, S. J.; Jung, J. T.; Wang, H. H.; Ali, A.; Quist-Jensen, C. A.; Macedonio, F.; Drioli, E.; Lee, Y. M. Lithium recovery from artificial brine using energy-efficient membrane distillation and nanofiltration. *Journal of Membrane Science* **2020**, *598*, 117683.

(4) Nie, X. Y.; Sun, S. Y.; Sun, Z.; Song, X.; Yu, J. G. Ion-fractionation of lithium ions from magnesium ions by electrodialysis using monovalent selective ion-exchange membranes. *Desalination* **2017**, *403*, 128–135.

(5) Williams, A. E.; McKibben, M. A. A brine interface in the Salton Sea Geothermal System, California: Fluid geochemical and isotopic characteristics. *Geochimica et Cosmochimica Acta* **1989**, *53*, 1905–1920.

(6) Goon, G. S.; Labban, O.; Foo, Z. H.; Zhao, X.; Lienhard, J. H. Deformation-induced cleaning of organically fouled membranes: Fundamentals and techno-economic assessment for spiral-wound membranes. *Journal of Membrane Science* **2021**, *626*, 119169.

(7) Geraldes, V.; Brites Alves, A. M. Computer program for simulation of mass transport in nanofiltration membranes. *Journal of Membrane Science* **2008**, *321*, 172–182.

(8) Wang, R.; Lin, S. Pore model for nanofiltration: History, theoretical framework, key predictions, limitations, and prospects. *Journal of Membrane Science* **2021**, *620*.

(9) Yaroshchuk, A.; Bruening, M. L.; Zholkovskiy, E. Modelling nanofiltration of electrolyte solutions. *Advances in Colloid and Interface Science* **2019**, *268*, 39–63.

(10) Foo, Z. H.; Rehman, D.; Coombs, O. Z.; Deshmukh, A.; Lienhard, J. H. Multicomponent Fickian solution-diffusion model for osmotic transport through membranes. *Journal of Membrane Science* **2021**, *640*, 119819.

(11) Wijmans, J. G.; Baker, R. W. The solution-diffusion model: a review. *Journal of Membrane Science* **1995**, *107*, 1–21.

(12) Epsztein, R.; Shaulsky, E.; Dizge, N.; Warsinger, D. M.; Elimelech, M. Role of Ionic Charge Density in Donnan Exclusion of Monovalent Anions by Nanofiltration. *Environmental Science and Technology* **2018**, *52*, 4108–4116.

(13) Lu, C.; Hu, C.; Ritt, C. L.; Hua, X.; Sun, J.; Xia, H.; Liu, Y.; Li, D.-W.; Ma, B.; Elimelech, M.; Qu, J. In Situ Characterization of Dehydration during Ion Transport in Polymeric Nanochannels. *Journal of the American Chemical Society* **2021**, *143*, 14242–14252.

(14) Malmir, H.; Epsztein, R.; Elimelech, M.; Haji-Akbari, A. Induced Charge Anisotropy: A Hidden Variable Affecting Ion Transport through Membranes. *Matter* **2020**, *2*, 735–750.

(15) Duignan, T. T.; Zhao, X. S. The Born model can accurately describe electrostatic ion solvation. *Physical Chemistry Chemical Physics* **2020**, *22*, 25126–25135.

(16) Labban, O.; Liu, C.; Chong, T. H.; Lienhard, J. H. Fundamentals of low-pressure nanofiltration: Membrane characterization, modeling, and understanding the multi-ionic interactions in water softening. *Journal of Membrane Science* **2017**, *521*, 18–32.

(17) Bird, R. B.; Klingenberg, D. J. Multicomponent diffusion-A brief review. *Advances in Water Resources* **2013**, *62*, 238–242.

(18) Tow, E. W.; Lienhard, J. H. Quantifying osmotic membrane fouling to enable comparisons across diverse processes. *Journal of Membrane Science* **2016**, *511*, 92–107.

(19) Chan, E. P.; Frieberg, B. R.; Ito, K.; Tarver, J.; Tyagi, M.; Zhang, W.; Coughlin, E. B.; Stafford, C. M.; Roy, A.; Rosenberg, S.; Soles, C. L. Insights into the Water Transport Mechanism in Polymeric Membranes from Neutron Scattering. *Macromolecules* **2020**, *53*, 1443–1450.

(20) Yaroshchuk, A.; Bruening, M. L.; Licón Bernal, E. E. Solution-Diffusion-Electro-Migration model and its uses for analysis of nanofiltration, pressure-retarded osmosis and forward osmosis in multi-ionic solutions. *Journal of Membrane Science* **2013**, *447*, 463–476.

(21) Wilson, A. D.; Lee, H.; Stetson, C. Local stress within a granular molecular solvent matrix, a mechanism for individual ion hydration. *Journal of Molecular Liquids* **2022**, 119544.

(22) Marcus, Y. The solvation number of ions obtained from their entropies of solvation. *Journal of Solution Chemistry* **1986**, *15*, 291–306.

(23) Richards, L. A.; Schäfer, A. I.; Richards, B. S.; Corry, B. Quantifying barriers to monovalent anion transport in narrow non-polar pores. *Physical Chemistry Chemical Physics* **2012**, *14*, 11633–11638.

(24) Liu, S.; Ganti-Agrawal, S.; Keten, S.; Lueptow, R. M. Molecular insights into charged nanofiltration membranes: Structure, water transport, and water diffusion. *Journal of Membrane Science* **2022**, *644*, 120057.

(25) Kingsbury, R. S.; Wang, J.; Coronell, O. Comparison of water and salt transport properties of ion exchange, reverse osmosis, and nanofiltration membranes for desalination and energy applications. *Journal of Membrane Science* **2020**, *604*, 117998.

(26) Hussain, S.; Haji-Akbari, A. Studying rare events using forward-flux sampling: Recent breakthroughs and future outlook. *Journal of Chemical Physics* **2020**, *152*, 60901.

(27) Taylor, R.; Krishna, R. *Multicomponent mass transfer*; Wiley, 1993; p 579.

(28) Ranjan Puhan, M.; Sutariya, B.; Karan, S. Revisiting the alkali hydrolysis of polyamide nanofiltration membranes. *Journal of Membrane Science* **2022**, *661*, 120887.